

See discussions, stats, and author profiles for this publication at: <https://www.researchgate.net/publication/359267502>

# Computational Modeling and Physics-Informed Machine Learning of Metal Additive Manufacturing: State-of-the-Art and Future Perspective

Article in *Annual Reviews of Heat Transfer* · January 2022

DOI: 10.1615/AnnualRevHeatTransfer.2022041733

CITATIONS

4

READS

237

2 authors, including:



Rahul Sharma

Rutgers, The State University of New Jersey

8 PUBLICATIONS 31 CITATIONS

SEE PROFILE

## CHAPTER 8

# COMPUTATIONAL MODELING AND PHYSICS-INFORMED MACHINE LEARNING OF METAL ADDITIVE MANUFACTURING: STATE-OF-THE-ART AND FUTURE PERSPECTIVE

**R. Sharma & Y.B. Guo\***

Department of Mechanical and Aerospace Engineering, New Jersey Advanced Manufacturing Institute, Rutgers University-New Brunswick, Piscataway, NJ

\*Address all correspondence to: Y.B. Guo, E-mail: yuebin.guo@rutgers.edu

*Metal additive manufacturing (AM) processes, such as powder bed fusion and directed energy deposition, involves very complex thermal dynamics phenomena including repetitive rapid heating, fast solidification, and melt-back, which are not encountered in conventional manufacturing processes, such as casting, forging, and heat treatment. Understanding and predicting the thermal behaviors in metal AM remain one central challenge for printing high-quality metal parts. This paper presents a systematic analysis of the state of the art in physics-based computational modeling, data-driven machine learning (ML) modeling, and physics-informed ML modeling for metal AM processes. The physical laws, recent developments, and limitations in modeling metal AM processes are analyzed in depth for the physics-based computational methods including computational fluid dynamics, finite volume method, finite element method, lattice Boltzmann method, and discrete particle method. The complementary pure data-driven ML and physics-informed machine learning methods and applications in metal AM are also reviewed. The key findings, common challenges, research needs, and an outlook regarding new and emerging modeling methods are outlined, which may serve as a roadmap for the computational AM community for future synergy that enables smart metal AM.*

**KEY WORDS:** metal additive manufacturing, process physics, computational model, machine learning, physics-informed machine learning

## 1. INTRODUCTION

### 1.1 Metal Additive Manufacturing (AM)

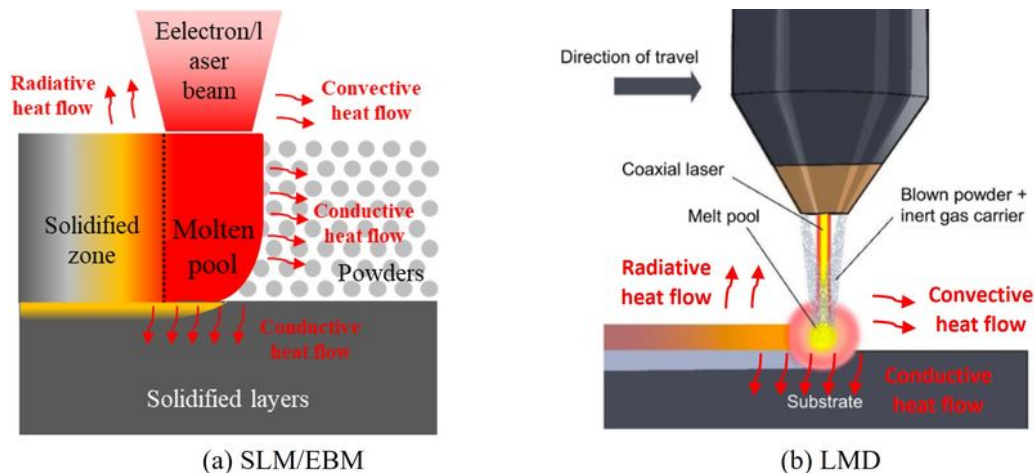
Metal AM builds three-dimensional (3D) parts by melting metal powders, layer by layer, directly from a digital model. Compared to traditional subtractive manufacturing processes (e.g., machining), metal AM offers a new enabling opportunity for making complex metal parts with design freedom, short development time, and environmental sustainability. For these reasons, metal AM is now widely accepted as a new paradigm for the design and production of high-performance components for aerospace, medical, energy, and automotive applications. The metal AM processes fall into two categories defined by ASTM Standard F2792<sup>1</sup> as powder bed fusion (PBF) and directed energy deposition (DED), as shown in Table 1. The distinction between PBF and DED lies in the configuration of the energy

**TABLE 1:** Key metal additive manufacturing processes

Processes	Acronyms	ASTM category	Institutions	Invention year	Refs.
Selective laser sintering	SLS	PBF	UT Austin	1989	3
Selective laser melting	SLM	PBF	Fraunhofer ILT	1995	4
Electron beam melting	EBM	PBF	Arcam AB	1997	5
Laser metal deposition	LMD	DED	Sandia Lab	1996	6

beam and powder delivery. PBF systems use an energy beam (e.g., laser or electron) to selectively fuse metallic powders on a bed, whereas DED uses an energy beam to fuse metal powders by melting as they are being deposited, based on ASTM 52900.<sup>2</sup> Major PBF processes include selective laser sinter (SLS), selective laser melting (SLM), and electron beam melting (EBM). The DED process cluster includes laser metal deposition (LMD), laser engineered net shaping (LENS), or laser cladding. Most of these names under the DED category are trademarks of different machine manufacturers; see Table 1.<sup>3–6</sup>

Figure 1 shows the process schematics and heat transfer for the typical PBF and DED processes. For SLM,<sup>7</sup> a fine powder delivering system is used to place a 20–50  $\mu\text{m}$  thick powder layer onto a substrate inside the building chamber filled with inert gas (usually argon gas) to prevent oxidations during melting and solidification. A laser beam selectively melts the powder by following a toolpath generated from a computer-aided design file of the part being produced. After the completion of one layer, the build platform will move downward at a distance equal to the thickness of one layer and a new layer of powder will be deposited. This cycle repeats itself until the whole part is built. SLS is like SLM conceptually, except that the material is being sintered in its solid state instead of being liquified as it is in SLM. Compared to SLM and SLS, EBM uses an electron beam as the

**FIG. 1:** Schematics of PBF and DED processes and heat transfer

heat source instead of a laser, and a vacuum chamber instead of inert gas.<sup>8</sup> Unlike PBF, DED does not need an enclosed build chamber since the material is fed by an inert gas stream, which prevents oxidation at the melt pool.<sup>9</sup> The laser- or electron beam-generated heat is dissipated through conduction to the powers and solidified layers, and convection and radiation into the environment.

The changes in the material during a metal AM process are driven by the thermal transport, which also determines the heat input needed to achieve the desired process. It is critical to link the thermal transport with the printing defects (e.g., porosity, heterogenous microstructure, and residual stress) to improve product quality and productivity<sup>10–15</sup> and achieve optimization.<sup>16</sup>

## 1.2 Melt Pool Dynamics

Metals processed by PBF and DED experience a completely different thermal transport when compared with conventional manufacturing and materials processing such as casting, forging, coating, and heat treatment.<sup>10–15</sup> For example, a comparison of the different thermal cycles is shown in Fig. 2. The unique thermal cycle in SLM is characterized by repetitive rapid heating, fast solidification, and melt-back.<sup>17</sup> The dynamics of the metal pool are attributed to three types of process variations:

- I. Complex part design: Parts' fine geometric features, such as thin walls, small holes, overhangs, create overheating, affect melt pool instability, and increase melt pool size<sup>18–21</sup> due to the less conductive powders than solids.<sup>22–26</sup>
- II. Nonuniform heat dissipation: The heat dissipation rates and mechanisms from the melt pool to the surrounding media are very different due to different thermal properties of the involved materials. For example, the heat loss to the powders is much

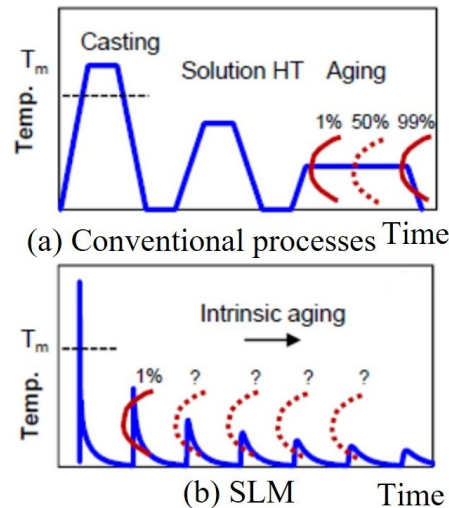


**FIG. 2:** Unique thermal cycles

less than that of the solid substrate due to the lower thermal conductivity of powders than solids. The major heat dissipation mechanism to the inert gas environment in the chamber is convection rather than conduction, which also contributes to different heat dissipations.

- III. Diverse scanning patterns: In addition to part geometric features and material thermal properties, process parameters (e.g., laser power, speed, and scan vector length) and different scanning patterns also have a significant impact on the thermal history of the melt pool.

In summary, the collective impact of complex part geometry, nonuniform heat dissipation, and diverse scanning patterns will cause a local nonuniform melt pool in terms of size and thermal history (e.g., cooling rate and thermal gradients), particularly in the surface layer zone, which leads to poor surface finish, large dimensional error, and high residual stress,<sup>22–26</sup> and microstructure heterogeneity.<sup>27–31</sup> Therefore, understanding and prediction of metal pool behavior remain central challenges for printing high-quality metal parts.

### 1.3 Computational Modeling of Metal AM

Physical models (e.g., analytical and computational) of metal AM are based on underlying physical principles of relevant processes, which provide explicit insights into the involved thermal phenomena and predict the process performance.<sup>32–35</sup> Computational methods, such as finite element method (FEM), computational fluid dynamics (CFD), and finite volume method (FVM), are in particular capable of handling multiscale (both length and time) and the multi-physics of complex metal AM processes, where more than 50 process variables are simultaneously responsible for process phenomena and part quality. For metal AM processes, microscale thermomechanical, micro-/mesoscale structural, and macroscale part modeling techniques (Fig. 3<sup>36</sup>) have demonstrated effectiveness in estimating thermal history and thermal gradients involved to minimize part distortion (dimensional accuracy) and tune thermomechanical properties (melt pool thermal gradient and surface integrity).

It is important to recognize that computational modeling methods are suffering three major inherent limitations, as follows:

- I. These models are based on assumptions, simplifications, and approximations in terms of output metrics generated.<sup>37</sup> While the past decade has seen significant advancement in the development of novel modeling techniques, most of the existing computational models manifest limited coherence with data from actual metal AM processes due to underlying assumptions, which span from domain-related limitations, i.e., laser/material interaction characteristics (e.g., absorptivity, optical penetration into the powder/bulk material), to material properties (e.g., thermal conductivity, heat capacity, coefficient of thermal expansion, density, and phase transition temperature).<sup>37</sup> Furthermore, multiscale (in terms of both space and time) integration over associated temperature ranges also introduces variability when predicting AM process characteristics.

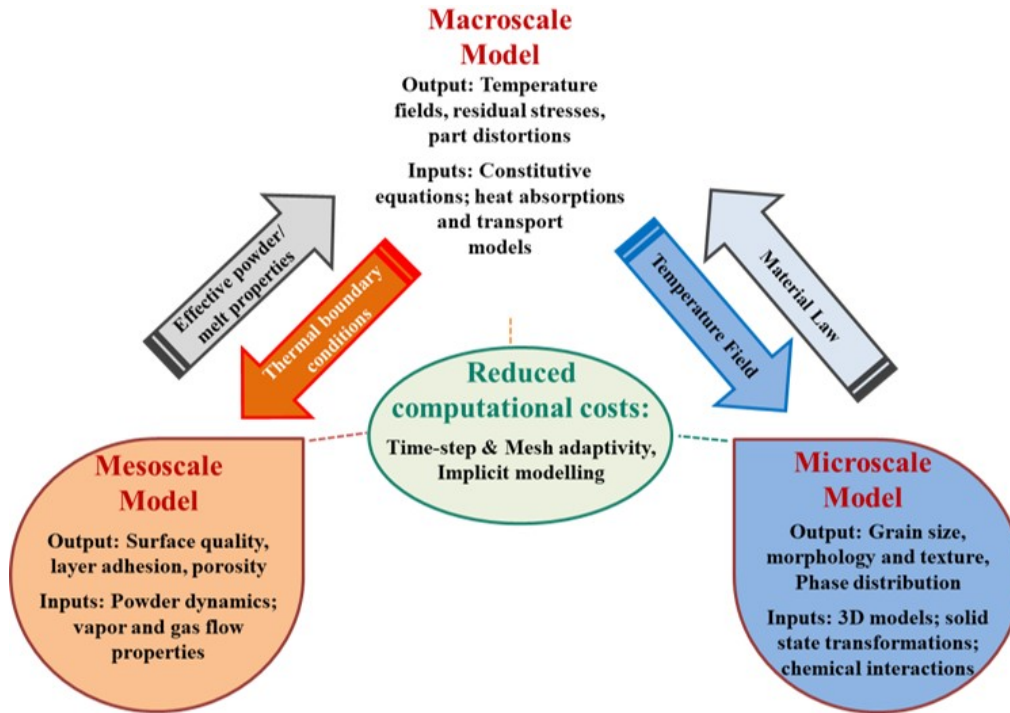


**FIG. 3:** Interrelationship between metal AM models at macro-, meso-, and microscale (adapted from Meier et al.<sup>36</sup>)

- II. Model coefficients corresponding to the nonlinear dynamic state of a metal AM process must be adapted when the process state changes. An online capability to continuously and recursively estimate the process model coefficients is highly desirable.
- III. The computational cost is exceedingly high for multiscale and multi-physics simulations, in particular, at the part level.

With the increasingly available data from online sensing during an AM process, surrogate data-driven modeling, such as machine learning (ML) and deep learning (DL), presents a promising method to harness the rich sensor data for discovering hidden patterns and predicting thermal phenomena.<sup>7,38–43</sup> In recent years, ML has gained prevalence in metal AM as a means of process modeling and optimization.<sup>44</sup> The advantages of ML are threefold. First, ML models can be computationally efficient once properly trained<sup>45</sup> thus providing a good fit for analyzing dynamic thermomechanical phenomena<sup>46</sup> in metal AM processes. Second, ML methods do not pose restrictive assumptions on the processes being analyzed<sup>47–49</sup> and are thus adaptable to a broad range of process variability. Third, data-driven models are transferable and generalizable,<sup>50</sup> as the basic structure of pre-trained models can be retained and updated using new data before being transferred to other AM processes that are suited for analysis using the updated ML models.<sup>51,52</sup> However, how to

leverage the respective advantages of data-driven models and conventional physics-based computational models for improving prediction accuracy, computation efficiency, and interpretability is a great challenge.

This paper presents a systematic review of the state of the art in physics-based computational modeling, data-driven ML modeling, and physics-informed ML modeling for metal AM processes with the aim to provide a roadmap to researchers in the computational AM community for future synergy that enables smart metal AM. The rest of this paper is organized as follows. Section 2 focuses on physics-based computational modeling including CFD, FEM, lattice Boltzmann method (LBM), and discrete particle method (DPM) methods and recent model development. Section 3 addresses data-driven ML, DL, and physics-informed machine learning (PIML) methods and key results. Section 4 summarizes key findings, shares challenges, and provides an outlook for future directions.

## 2. PHYSICS-BASED COMPUTATIONAL MODELING

### 2.1 Computational Fluid Dynamics Modeling in Liquid Domain

In PBF, the layer of metal powder is scanned by either a laser or electron beam heat source. The heat source converts the metal powder to liquid, which eventually solidifies and converts to the final product. There are multiple physics involved in this process, which has a significant effect on the melt pool shape and size. Furthermore, melt pool size and cooling rate result in different microstructure and mechanical properties of the component. The development of a computational model that replicates the actual AM process by incorporating all the physics involved in the process is very important to save the cost of expensive experiments.

The PBF process starts with the absorption of heat energy by the powder particles, which results in a phase change from powder to liquid. There is liquid flow in the melt pool due to density difference, surface tension, and gravitational force.<sup>53</sup> Due to the dependence of the surface tension coefficient on temperature, there is Marangoni convection on the liquid–gas interface.<sup>54</sup> The recoil pressure due to material evaporation changes the melt pool size when the temperature of the material reaches above the evaporation temperature (Fig. 4).<sup>55</sup> Heat transfer from the melt pool to surrounding powder particles and gas can take place in the form of conduction, convection, and radiation. Furthermore, when the moving heat source moves away from the particular location, solidification starts and there is a phase change of metal from liquid to solid. These complex physical phenomena depend on the process parameters, such as heat source power, scanning speed, and powder properties, which eventually influence the quality of the final product.

#### 2.1.1 Volume-Of-Fluid (VOF) Method

In a PBF process, especially selective laser melting, the material exists in three different phases at different times. Firstly, powder particles convert to liquid during the scanning by the heat source. Generally, in an SLM process, the temperature of material crosses the evaporation temperature of the material after which liquid metal converts to vapor phase.

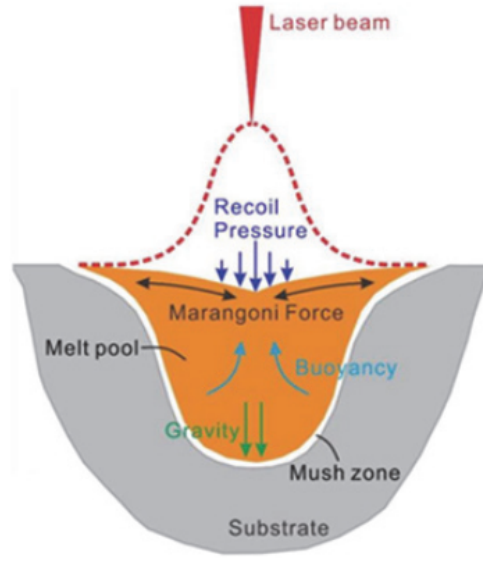


**FIG. 4:** Different forces acting on the melt pool

Moreover, inert gas also exists in the SLM chamber during the operation. To assign correct material properties to different phases during simulation, it is very important to track the interface between the different materials. The VOF method is used by most researchers to track the interface between two immiscible phases.<sup>54,56–59</sup> In this method, the interface is not explicitly defined or tracked but is reconstructed based on the volume fraction of phase 1 (liquid) in each cell. In VOF, a single set of momentum equations is shared by different fluids and the VOF of each fluid is tracked down throughout the whole domain. The basic idea for this method is to define a phase 1 (liquid) fraction  $\alpha$  for the whole mesh. The value of  $\alpha$  is 1 in a grid cell if the cell contains only phase 1 (liquid);  $\alpha = 0$  if the cell does not have phase 1 at all; and  $0 < \alpha < 1$  if the cell contains partial phase 1 (Fig. 5). After that, the liquid fraction  $\alpha$  is advected throughout the domain with the local flow velocity. The governing equation<sup>60</sup> to calculate the interface is given as follows:

1	1	1	1	0.8
1	1	1	1	0.3
1	1	1	0.9	0.05
1	1	0.9	0.1	0
1	0.85	0.05	0	0

**FIG. 5:** Value of liquid fraction in different cells



$$\frac{\partial \alpha}{\partial t} + \nabla \cdot (\alpha u) = 0 \quad (1)$$

It can be inferred from Eq. (1) that  $\alpha$  moves with the fluid velocity in space and time. The initial condition is given by stating the initial free surface shape.

### 2.1.2 Governing Equations

To capture the fluid flow in the melt pool, Navier-Stokes equations (mass and momentum conservation equations) are solved in the computational domain.<sup>54,56–58,61</sup> The phase boundary of liquid and gas is captured by the VOF method. To successfully capture the physical phenomenon in simulation, temperature-dependent material properties should be used in the simulation, as follows:

$$\frac{\partial (\rho \vec{u})}{\partial t} + \vec{u} \cdot \nabla (\rho \vec{u}) = -\nabla p + \nabla \cdot \vec{\tau} + \rho \vec{g} + \vec{F}_c + \vec{F}_s + \vec{F}_m + \vec{F}_r \quad (2)$$

The left side of Eq. (2) represents inertial force per unit volume on the fluid, and the right side gives the sum of the pressure gradient force represented as the gradient of pressure  $p$ , viscous force represented as the divergence of viscous stress  $\tau$ , and body force per unit volume incorporate through acceleration due to gravity  $g$ . Darcy's term from the Carman–Kozeny equation  $F_c$ , the capillary force of the surface tension  $F_s$ , the thermocapillary (Marangoni) force  $F_m$ , and the recoil force  $F_r$  are incorporated as the source terms in the standard Navier-Stokes equation. The viscous stress can be related to the strain rate tensor by assuming the fluid in the melt pool to be the Newtonian fluid, as follows:

$$\vec{\tau} = 2\mu \left( \frac{1}{2} \nabla \vec{u} + \frac{1}{2} (\nabla \vec{u})^T \right) - \frac{1}{3} (\nabla \cdot \vec{u}) I \quad (3)$$

Darcy's term from the Carman–Kozeny equation represents the sink term, which helps in lowering the velocity of the fluid at the solid–liquid phase transition zone and applies an effective pressure drop when the fluid flow is solved in the solid domain.<sup>54</sup> Also, this term reduces to zero in the melted region, as follows:

$$\vec{F}_c = - \frac{(1 - \beta)^2}{\beta^3 + \omega} C \vec{u} \quad (4)$$

where  $C$  is the mushy zone constant and a high value is used in the models;  $\omega$  is a very small constant used to prevent division by zero when the liquid fraction  $\beta$  becomes zero in the un-melted region. The negative sign indicates that the sink term is opposite to the direction of the melting flow.

$$\beta = \begin{cases} 0, & T < T_{\text{solidus}} \\ \frac{T - T_{\text{solidus}}}{T_{\text{liquidus}} - T_{\text{solidus}}}, & T_{\text{solidus}} \leq T < T_{\text{liquidus}} \\ 1, & T \geq T_{\text{liquidus}} \end{cases} \quad (5)$$

The surface tension  $F_s$  and the thermocapillary (Marangoni) force  $F_m$  on the melt pool interface between liquid and gaseous phase,<sup>54</sup> as follows:

$$\vec{F}_s = \sigma \kappa \delta \vec{n}, \quad \vec{F}_m = \frac{d\sigma}{dT} [\nabla T - \vec{n}(\vec{n} \cdot \nabla T)] \quad (6)$$

$$\kappa = \nabla \cdot \vec{n} \quad (7)$$

where  $\sigma$  is the temperature-dependent surface tension coefficient of the metallic phase (measured in N/m),  $\kappa$  is the curvature (measured in 1/m),  $T$  is the temperature,  $n$  is the unit vector normal to the interface, and  $\delta$  acts like a delta function to capture the location of the interface.

When the temperature in the melt pool is higher than the vaporization temperature  $T_{\text{vap}}$  of the metal, the metal escapes from the metallic phase to the surrounding gaseous phase and provides a recoil force due to evaporation,<sup>54</sup> as follows:

$$\vec{F}_r = p_{\text{sat}} \delta \vec{n}, \quad p_{\text{sat}} = p_0 \exp \left[ \frac{L_{\text{vap}}}{R} \left( \frac{1}{T_{\text{vap}}} - \frac{1}{T} \right) \right] \quad (8)$$

where  $p_0$  is the atmospheric pressure,  $L_{\text{vap}}$  is the latent heat from the liquid phase to the vapor phase, and  $R$  is the gas constant (8.314 J/K mol).

To calculate temperature, the energy balance equation is solved in the computational domain,<sup>54</sup> as follows:

$$\frac{\partial(\rho h)}{\partial t} + \nabla \cdot (\rho \vec{u} h) = \nabla \cdot (k \nabla T) + Q_{\text{las}} + Q_{\text{conv}} + Q_{\text{rad}} + Q_{\text{vap}} \quad (9)$$

There are four source/sink terms used in the standard energy conservation equation.  $Q_{\text{las}}$  represents the laser energy input,  $Q_{\text{con}}$  and  $Q_{\text{rad}}$  represent the convective and radiative heat losses respectively, and  $Q_{\text{vap}}$  is the evaporative cooling. Here the enthalpy  $h$  and conductivity  $k$  represent the combined mixture value and can be computed as follows:

$$h = \int_0^t C dT = \frac{\rho_m \alpha_m C_m + \rho_g (1 - \alpha_m) C_g}{\rho} \quad (10)$$

$$k = \alpha_m k_m + (1 - \alpha_m) k_g \quad (11)$$

where the subscripts  $m$  and  $g$  represent the corresponding properties of the metallic and gaseous phases, respectively. Furthermore, the metallic phase has metal in the liquid or solid phase. Therefore,  $C_m$  can be computed as follows:

$$\begin{cases} C_m = C_m(T) & \text{if } T < T_S \text{ and } T > T_L \\ C_m = C_m(T) + \frac{(T - T_S)}{(T_L - T_S)} L_{\text{melt}} & \text{if } T_S < T < T_L \end{cases} \quad (12)$$

where  $L_{\text{melt}}$  represents the latent heat of material when the phase changes from the solid phase to the liquid phase.

When the temperature in the process reaches more than the evaporation temperature of the material, evaporative cooling must be considered in the domain,<sup>54</sup> as follows:

$$Q_{\text{vap}} = \dot{m}_{\text{vap}} L_{\text{vap}} \delta, \quad \dot{m}_{\text{vap}} = p_{\text{sat}} \sqrt{\frac{m}{2\pi k_b T}} \quad (13)$$

where  $\dot{m}_{\text{vap}}$  is the evaporation flux,  $L_{\text{vap}}$  is the latent heat from the liquid phase to the vapor phase, the saturated pressure  $p_{\text{sat}}$  can be defined from Eq. (8),  $k_b$  is the Boltzmann constant ( $1.38 \times 10^{-23}$  J/K), and  $m$  is the molecular weight. This term works like a large sink term when the temperature reaches close to the evaporation temperature of the material and suppresses a further rise in temperature. The presence of  $\delta$  in Eq. (13) emphasizes that the corresponding heat transfer only occurs within the mixture interfaces. The equations for  $Q_{\text{las}}$ ,  $Q_{\text{con}}$ , and  $Q_{\text{rad}}$  are defined in the following sections.

### 2.1.3 CFD Models for Microscale Fluid Dynamics

The coupled thermal and fluid model is a very important tool for understanding metal AM process physics. Selecting incorrect process parameters could lead to porosity, non-molten powder, distortion, and layers that are not fully connected. As a result, it affects the strength and performance of the final product. Although experiments can be performed to calculate the optimal process parameters by using empirical relations between parameters, these experiments are very expensive. Also, it is very difficult to thoroughly understand the complex physics involved in the process at a microscale. Therefore, many researchers have attempted to develop a mathematical model by coupling the energy balance equation with the Navier-Stokes equation to understand the evolution of temperature field and melt-pool dynamics at the microscale.

Li et al.<sup>58</sup> developed a 2D model to investigate the rapid melting and solidification process by using the VOF method to capture the interface. While the effect of surface tension is included in the model, the Marangoni and recoil forces were not taken into account. Gürtler et al.<sup>62</sup> developed a transient 3D model using a moving heat source to simulate the process dynamics of laser beam melting of metals using OpenFOAM. Although the model was simple (as it did not consider the effect of surface tension, Marangoni, and recoil force), it could reproduce the fundamental properties of the laser beam melting process. Furthermore, Tseng and Li.<sup>54</sup> studied the effects of surface tension, Marangoni, and recoil forces on the interfacial morphology for SLM (Fig. 6). The Marangoni flow increases the width of the melt pool by enhancing the heat transfer from the center of the laser focus region to the radially outward direction, and the surface tension force contributes to the periodic sloshing motions and oscillations of the height of the melt pool.

Panwisawas et al.<sup>56</sup> studied the evolution of pores during selective laser melting. With an increase in the laser scan speed, the morphology of pores was observed to change from near spherical to the elongated shape. When the laser heat source interacts with the smaller domain and flow velocity is in the opposite direction of gravitational force, spherical or ellipsoidal pores were formed; whereas, when the laser heat source interacts with

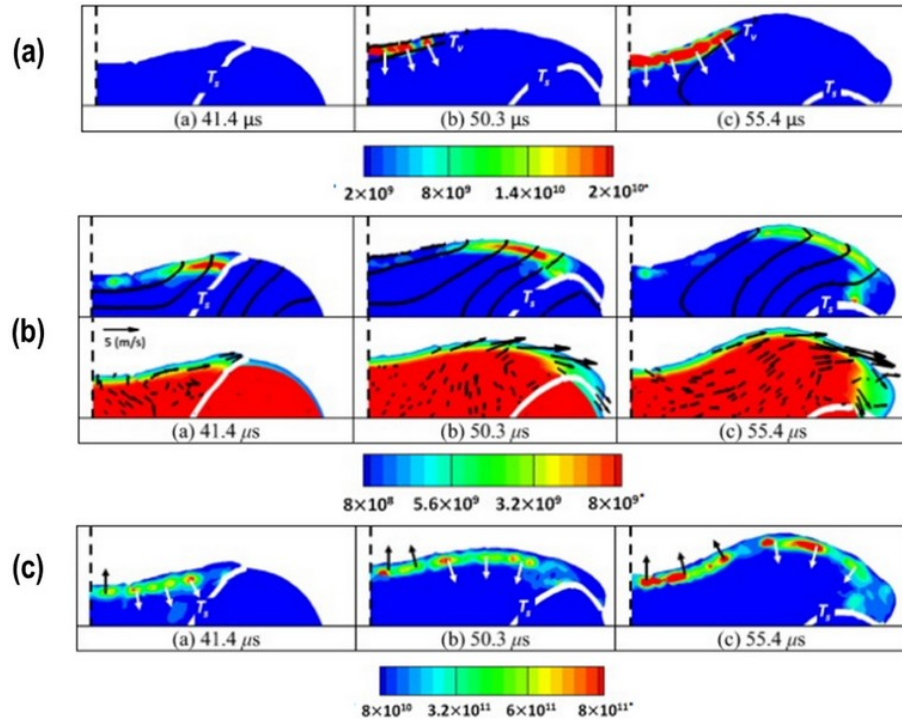


**FIG. 6:** Contours showing the magnitude of (a) recoil force, (b) Marangoni force, and (c) surface tension force (Reprinted with permission from Elsevier, Copyright 2019)<sup>54</sup>

the larger domain, flat or elongated pores were formed because of the tearing apart of two interspacing layers. De Baere et al.<sup>63</sup> developed a macro thermo-fluid numerical model of the SLM process and coupled it with a metallurgical submodel that could give the solidification parameters, such as temperature gradient, cooling rate, and growth velocity, and determined whether grains were columnar or equiaxed. The morphology was then used as an input for the microstructural model, which simulates the final microstructure after heat treatment. Panwisawas et al.<sup>57</sup> studied thermal fluid flow and the resulting microstructural evolution with different powder layer thicknesses and scanning speeds during SLM by developing a mesoscale model in OpenFOAM (Fig. 7). The high thermal gradient of SLM enables the columnar grain structure to be grown. However, it was found that the development of equiaxed grains has been suppressed during SLM due to very little time available for nucleation to start. Moreover, there is a change in thermal and solidification behavior of the melt pool upon changing the surrounding atmosphere from air to argon, but it does not significantly affect the morphology of the solidified tracks.

## 2.2 Finite Element Modeling in Continuum Domain

A finite element-based model is used by many researchers to predict the temperature field in the model and associated phenomena (such as residual stress, microstructure, and

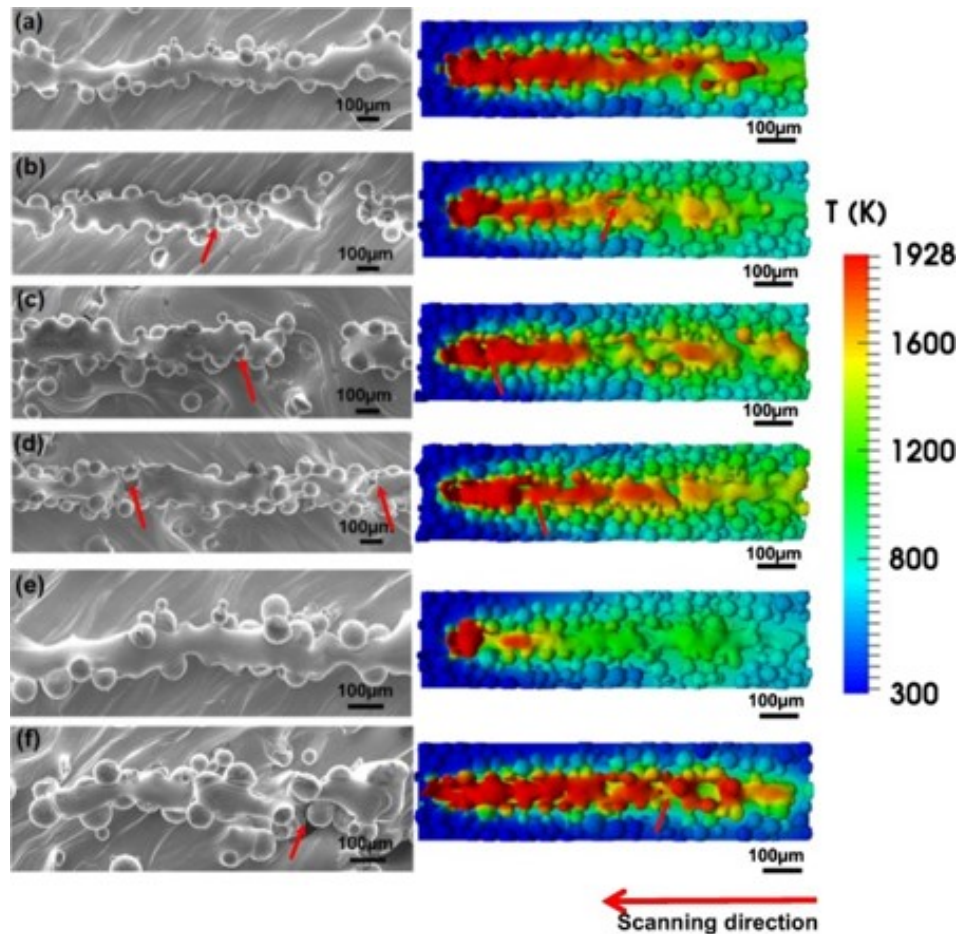


**FIG. 7:** Surface morphology (left) measured on the top view of the single track scanning and (right) predicted from thermal fluid dynamics calculation at different powder layer thicknesses: (a) 20  $\mu\text{m}$ , (b) 60  $\mu\text{m}$ , (c) 80  $\mu\text{m}$ , (d) 100  $\mu\text{m}$ , (e) argon effect, and (f) fast scanning speed ( $4 \times 10^3$  mm/s) effect at 20  $\mu\text{m}$  layer thickness. The arrows point to the presence of cavelike pores (Reprinted with permission from Elsevier, Copyright 2017).<sup>57</sup>

balling effect). It is difficult to capture melt-pool dynamics, temperature field and the resulting macroscale phenomena (such as thermal distortion) in one fully coupled model due to the very high computational cost. Many researchers attempted to couple the thermal model (without melt-pool dynamics) with the mechanical model to study the different macroscale phenomena in additive manufacturing processes. A successful finite element model requires temperature-dependent material properties of the material for the heating and cooling cycle, a thermal model representing heat input from the laser heat source to predict correct temperature field, and coupling of a thermal model with the mechanical model to predict stress and distortion.

### 2.2.1 Heat Flux Modeling Methods

The heat source model is used in a computational model to include the heat energy distribution from the heat source. It affects the thermal-fluid flow phenomena and powder-liquid-solid phase transition during the process. Therefore, the heat source model is the key to correctly simulate and analyze the powder-based fusion AM process. Generally, the surface Gaussian heat source model is used by researchers, because the powder layer thickness is very thin and most of the heat is absorbed, up to a few nanometers. For the surface heat source model, all the energy absorption occurs only on the top surface and further heat transfer in the powder bed and bulk solid occurs through conduction. This however overlooks the particle nature of the powder bed. The powder bed particles cause internal reflection and scattering of the incident beam energy, as shown in Fig. 8.<sup>64</sup> This results in volumetric absorption of the incident energy in the powder bed, which emphasizes the use of volumetric heat source models in the modeling and simulation of the SLM process. Various types of heat flux models used in different studies were summarized<sup>65</sup> (Table 2<sup>66-74</sup>).

### 2.2.2 Heat Transfer Equations (Conduction, Convection, and Radiation)

The continuum energy conservation equation is solved to obtain the temperature field in the domain.<sup>75-78</sup> The governing equation for transient heat transfer for a component is given as follows:

$$\frac{\partial(\rho h)}{\partial t} = \nabla \cdot (k \nabla T) + Q_{\text{las}} + Q_{\text{conv}} + Q_{\text{rad}} \quad (14)$$

where  $\rho$  is the material density,  $h$  is the enthalpy of the material,  $k$  is the conductivity of the material,  $T$  is the temperature, and  $Q_{\text{las}}$ ,  $Q_{\text{con}}$ , and  $Q_{\text{rad}}$  are the heat input from the heat source, convective heat loss, and radiative heat loss, respectively

$$q = \frac{2AP}{\pi R^2} \exp\left(-\frac{2(x-vt)^2}{R^2}\right) \quad (15)$$

$$q_{\text{conv}} = h(T - T_{\text{ref}}) \quad (16)$$

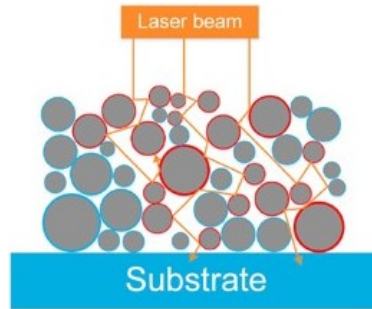


**FIG. 8:** Reflection of laser beam in powder (Reprinted with permission from Elsevier, Copyright 2019)<sup>64</sup>

TABLE 2: Representative heat flux models

Heat flux types	Heat flux equations	Notes	Refs.
Surface (2D) heat flux	$q(x, y) = \frac{2P}{\pi b^2} \exp\left(-\frac{2(x^2 + y^2)}{b^2}\right)$	2D Gaussian distribution of surface heat flux	66
	$I(x, y) = a(x, y) \frac{P}{R^2} \exp\left(-\frac{x^2 + y^2}{R^2}\right)$	2D Gaussian distribution of surface intensity, absorptivity included	67
	$q = \frac{P\eta d}{\pi r_{lb}^2} \exp\left(-\frac{dr^2}{r_{lb}^2}\right)$	2D Gaussian distribution of surface heat flux, beam distribution parameter included	68
	$I(x, y) = \frac{(1-R)P}{\pi w l} \exp\left(-\frac{x'^2}{w^2} - \frac{y'^2}{l^2}\right)$	Elliptical laser intensity	69
Volumetric (3D) heat flux	$S_0 = I_0 \delta(1 - r_f) \exp(-\delta z) \times \exp\left(-x^2 + \frac{z^2}{a^2}\right)$	Volumetric heat source, absorption depth, Gaussian parameter included	70
	$S_0 = I_0 \delta(1 - r_f) \exp(-\delta z) \times \exp\left[-\left(\beta^2 + \frac{r}{a}\right)\right] f(t)$	Volumetric heat source, absorption depth, density parameter included	71
Conical (3D) heat flux	$q_v(x, y, z) = (9Q_v)(\pi h r_0^2) \times \exp\left[-\left(\frac{h^2}{(h-z)^2} 3 \frac{(x^2 + y^2)}{r_0^2}\right)\right]$	Conical shape volumetric heat flux for high penetration depth	72
	$q_v(x, y, z) = (9\eta P) \left[ \pi(1 - e^{-3})(z_e - z_i) \times (r_e^2 + r_e r_i + r_i^2) \right] \exp\left[-3(r^2/r_c^2)\right]$	Conical shape volumetric heat flux, distribution parameter of the cone as a function of depth included	73

TABLE 2: (continued)

Heat flux types	Heat flux equations	Notes	Refs.
Surface (2D) and volumetric (3D) heat flux of pulse laser	$I = I_0 f(r) f(t)$ $f(r) = \exp \left[ -2 \frac{(x - vt)^2}{r_0^2} \right]$ $f(t) = \begin{cases} 1, & 0 \leq t \leq t_p \\ 0, & t_p \leq t \leq \eta T_t \end{cases}$	Surface heat flux, time function used to simulate laser modulation	74
	$\begin{cases} P(f, m, t) = P_{\text{peak}}, & \text{if } \frac{N}{f} \leq t \leq \frac{m \cdot N + 1}{f \cdot m}, \\ & (N = 0, 1, 2, \dots) \\ P(f, m, t) = 0, & \text{if } \frac{m \cdot N + 1}{f \cdot m} < t < \frac{N + 1}{f}, \\ & (N = 0, 1, 2, \dots) \end{cases}$ $F(x, y, z, P) = \frac{A \cdot P(f, m, t)}{\pi \cdot R_0^2 \cdot h} \times \exp \left[ -3 \cdot \frac{(x - v_x \cdot t)^2 + (y - v_y \cdot t)^2}{r(z)^2} \right]$ $r(z) = R_0 - (R_0 - R_b) \cdot \frac{z}{h}, \quad R_b = D \cdot R_0$	Moving volumetric heat flux of a pulsed laser	65



$$q_{\text{rad}} = \varepsilon' \sigma' (T^4 - T_{\text{ref}}^4) \quad (17)$$

where  $A$  is the absorption coefficient,  $P$  is the laser heat source power,  $v$  is the laser scanning velocity,  $h$  is the convective heat transfer coefficient, and  $\varepsilon'$  is the emissivity of the powder and solid material.

### 2.2.3 Constitutive Equations

A coupled model is used by some researchers to calculate thermal residual stress by using the following governing equation:<sup>75,76,79,80</sup>

$$\frac{\partial S_{ij}}{\partial x_j} = 0 \quad (18)$$

The mechanical stress-strain constitutive law is given as follows:

$$S_{ij} = C_{ijkl} \varepsilon_{ij}^{\text{el}} \quad (19)$$

where  $C_{ijkl}$  is the stiffness matrix, which is a fourth-order tensor and  $\varepsilon^{\text{el}}$  is the elastic strain. The total strain,  $\varepsilon$  at a point, is given as follows:

$$S_{ij} = C_{ij}^{\sigma} + \varepsilon_{ij}^{\text{th}} \quad (20)$$

where  $\varepsilon^{\sigma}$  represents the mechanical strain and  $\varepsilon^{\text{th}}$  is the strain caused by thermal expansion. Also, the mechanical strain comprises elastic and plastic strain, which is mathematically represented as follows:

$$\varepsilon_{ij}^{\sigma} = \varepsilon_{ij}^{\text{el}} + \varepsilon_{ij}^{\text{pl}} \quad (21)$$

The strain caused by thermal expansion is given as follows:

$$\varepsilon_{ij}^{\text{th}} = \alpha (T - T_{\text{ref}}) \delta_{ij} \quad (22)$$

where  $\alpha$  is the coefficient of thermal expansion of the solid and  $\delta$  is the Kronecker's delta given as follows:

$$\delta_{ij} = \begin{cases} 0 & \text{if } i \neq j \\ 1 & \text{if } i = j \end{cases} \quad (23)$$

### 2.2.4 FEM Models at Part Scale

The prediction of the correct temperature field is a very crucial step in FE analysis as it affects the resulting phenomenon such as thermal stress and distortion. Childs et al.<sup>81</sup> studied the effects of laser power and scan speed on different types of track formation during SLM. Zhang et al.<sup>82</sup> proposed a combination of different parameters to achieve a high energy input in SLM. They concluded that high laser power, low scan velocity, narrow scan interval, and preheating result in greater energy input. Verhaeghe et al.<sup>55</sup> incorporated

the volume shrinkage in the numerical model through an iterative shrinkage routine to study the temperature field.

Thermal residual stress results in distortion of the part, which is one of the major defects in AM manufactured parts. It results in the change of dimensional accuracy and mechanical properties of the final component. Due to rapid heating and cooling, there is a high-temperature gradient that results in the generation of thermal stress. Thermal residual stress on the newly scanned layer has a tensile nature on the top layer, which converts to compressive with an increase in depth. A similar type of trend is observed in the substrate, also where tensile stress is developed on the free surface while compressive stress is developed on the end where a new layer is deposited (Fig. 9).<sup>83</sup> Nowadays, simulation is a powerful tool to predict the residual stresses in the component and optimize the process parameters before the actual manufacturing of the component. The only disadvantage of the fully coupled thermomechanical FE model is the high computation cost, because multiple physics are involved in the process. Various researchers developed the coupled thermomechanical models to calculate the residual stress at the microscale.<sup>84–88</sup> The simulation requires a very long time to solve, even for dimensions in micrometers with fine meshing. Therefore, predicting the stress for the full component at the macroscale is very difficult.

Some researchers took initiative and predicted residual stress at the macro-scale.<sup>89–92</sup> To calculate stress on a macroscale, it is very important to simulate a multi-layer buildup process. There are various techniques to simulate multiple layers in simulation. Multiple sequential steps, in which temperature from the previous step is imported for a newly added layer, were used by Ding et al.<sup>93</sup> The element “birth and death” technique was used by Roberts et al.<sup>77</sup> in which the addition of a new powder layer on the previously deposited layer is treated as the activation of new elements in the simulation at a particular time point. Dai and Shaw<sup>88</sup> simulated the buildup of the part by adding all the powder elements in one layer onto the previously deposited layer. Then, some of the newly added elements were subjected to laser processing in a predefined scanning strategy, which resulted in the

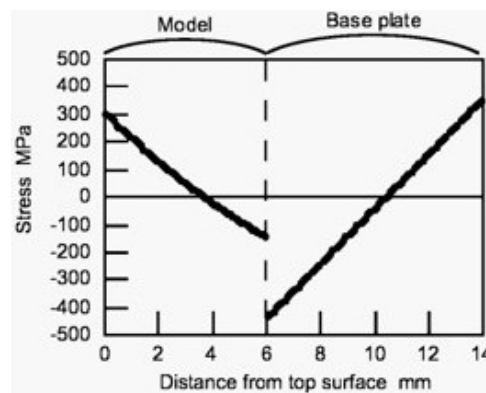


**FIG. 9:** Distribution of residual stress within model and base plate (Reprinted with permission from Elsevier, Copyright 2004)<sup>83</sup>

development of a full component surrounded by loosely held powder particles. Li et al. developed a geometry scalable predictive model across a microscale laser scan, mesoscale layer hatch, and macroscale part buildup to quickly predict residual stress in different scanning strategies.<sup>23–25</sup> The predictions were validated using the L-shaped bar and bridge structures (Fig. 10). The geometry scalability law provides an effective tool for optimizing part designs.

### 2.3 Lattice Boltzmann Method for Modeling Microscale Fluid Flow

Some researchers have employed lattice Boltzmann (LB) approach to simulate fluid dynamics for metal AM processes.<sup>94–103</sup> In this technique, fluid flow is determined by simulating the temporal evolution of distribution function  $f(\mathbf{x}, \mathbf{v}, t)$ , where  $f$  is the probability of finding a fluid atom at the position  $\mathbf{x}$  at time  $t$  and moving with the velocity  $\mathbf{v}$  rather than directly calculating velocity, and pressure as in Navier-Stokes equations. The distribution function  $f$  helps to calculate density and momentum in the computational domain, while the internal energy distribution function  $h$  helps to calculate the energy density of the model, as follows:

$$\rho = \sum_i f_i, \quad \rho \mathbf{u} = \sum_i \mathbf{e}_i f_i, \quad E = \sum_i h_i \quad (24)$$

where  $\rho$  is the density,  $f_i$  is the discretized distribution function,  $\mathbf{u}$  is the macroscopic velocity,  $\mathbf{e}_i$  is the velocity to the neighboring site, and  $h_i$  is the discretized internal energy distribution.

The governing equation to calculate the collision and displacement of the distributions is given by the equations of motion, as follows:

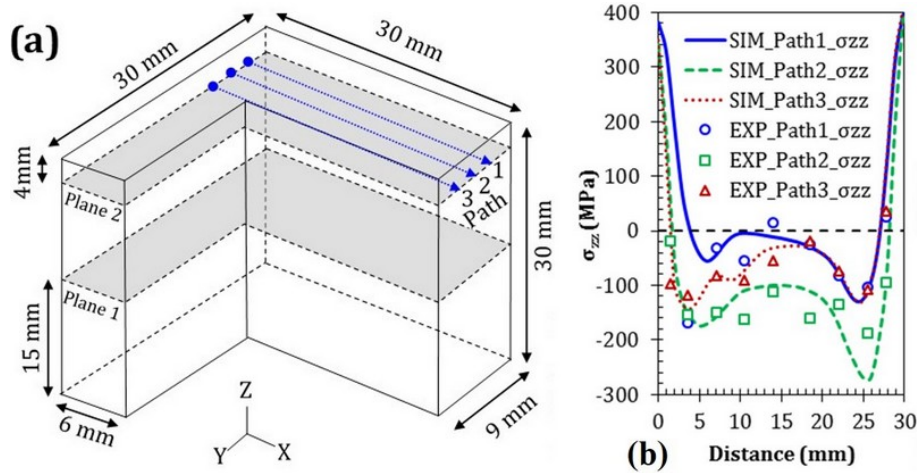


**FIG. 10:** Predicted and measured residual stress  $\sigma_{zz}$  profiles (Reprinted with permission from Elsevier, Copyright 2018)<sup>24</sup>

$$f_i(\mathbf{x} + \mathbf{e}_i \Delta t, t + \Delta t) - f_i(\mathbf{x}, t) = \frac{\Delta t}{\tau_f} (f_i^{\text{eq}}(\mathbf{x}, t) - f_i(\mathbf{x}, t)) + F_i \quad (25)$$

$$h_i(\mathbf{x} + \mathbf{e}_i \Delta t, t + \Delta t) - h_i(\mathbf{x}, t) = \frac{\Delta t}{\tau_h} (h_i^{\text{eq}}(\mathbf{x}, t) - h_i(\mathbf{x}, t)) \quad (26)$$

where  $\tau_f$  and  $\tau_h$  are the dimensionless relaxation times for the velocity and temperature field, respectively.  $f^{\text{eq}}$  and  $h^{\text{eq}}$  are the distributions functions at an equilibrium state, which depend on the speed of sound.<sup>104</sup> Equations (25) and (26) are solved in a two-step procedure, i.e., collision and advection.

Collision:

$$f_i^{\text{out}}(\mathbf{x}_i, t) = f_i^{\text{in}}(\mathbf{x}, t) + \frac{\Delta t}{\tau_f} (f_i^{\text{eq}}(\mathbf{x}, t) - f_i^{\text{in}}(\mathbf{x}, t)) + F_i \quad (27)$$

$$h_i^{\text{out}}(\mathbf{x}_i, t) = h_i^{\text{in}}(\mathbf{x}, t) + \frac{\Delta t}{\tau_h} (h_i^{\text{eq}}(\mathbf{x}, t) - h_i^{\text{in}}(\mathbf{x}, t)) \quad (28)$$

Advection:

$$f_i^{\text{in}}(\mathbf{x} + \mathbf{e}_i \Delta t, t + \Delta t) = f_i^{\text{out}}(\mathbf{x}_i, t) \quad (29)$$

$$h_i^{\text{in}}(\mathbf{x} + \mathbf{e}_i \Delta t, t + \Delta t) = h_i^{\text{out}}(\mathbf{x}_i, t) \quad (30)$$

where  $f^{\text{out}}$  and  $f^{\text{in}}$  denote the outgoing (e.g., after collision) and incoming (e.g., before the collision) distribution functions, respectively.

In the LBM, the development of a thermal model with a heat source and hydrodynamic model is important. Generally, a Gaussian-type heat source is used in the modeling.<sup>94,95</sup> For laser heat source processes, such as SLM, the surface heat source model is used as most of the laser intensity is reflected and laser intensity is mostly absorbed on the surface.<sup>96</sup> Melt-pool flow is driven by capillary, Marangoni forces, recoil pressure due to evaporation, and the wettability of the powder particles. Körner et al.<sup>97</sup> developed the numerical method based on the LBM approach, which is further explored by including free surface boundary conditions, surface tension, phase transitions, and wetting.<sup>98–100</sup> By using the LB approach, the influence of the wetting conditions on balling was studied by Körner et al.<sup>94</sup> It was found that the balling tendency will increase with a larger wetting angle. Additionally, it was found that the packing density and stochastic composition have a major influence on melt pool characteristics.

Körner et al.<sup>101</sup> investigated the surface quality of selective electron beam melted-manufactured (SEBM) vertical walls of Ti-6Al-4V as a function of beam power, scan speed, and layer thickness. It was found that the wall thickness increases with an increase in the ratio of beam power and scan speed. The extrusion was observed on the walls due to the balling mechanism. Körner et al.<sup>102</sup> investigated the dependence of grain structure on the process parameters during SEBM of IN718 by tracking the direction and magnitude of the temperature gradient through simulations. A columnar grain structure evolved in the build direction is changed to an equiaxed grain structure by modifying the line offset for hatching from 150 to 37.5  $\mu\text{m}$  and scan speed from 2.2 to 8.8 m/s at 594 W. Rai et al.<sup>103</sup> developed a 2D coupled cellular automaton (CA)—LB model to study the influence

of different melting strategies on the final grain structure. The coupling was done by interchanging the current temperature field and the phase state information. The LB model provides the temperature information applied to grain growth, and the CA model provides current phase information to the LB model as shown in Fig. 11.

## 2.4 Discrete Particle Method in Particle Domain

The discrete particle method is used by researchers to model metal AM in which instead of treating the material as a continuum medium, the focus is made on the individual powder particle. <sup>105–108</sup> In the discrete element approach, modeling is done in three steps: deposition of powder particles which takes care of the movement of the particles induced by contact with other neighboring particles as well as surface, laser heat energy input, and particle thermodynamics which takes care of temperature evolution as heat is transferred between particles through conduction. For deposition of particles, different forces are considered on the individual particle, and the equation of the particle is given by Newton's second law, as follows:

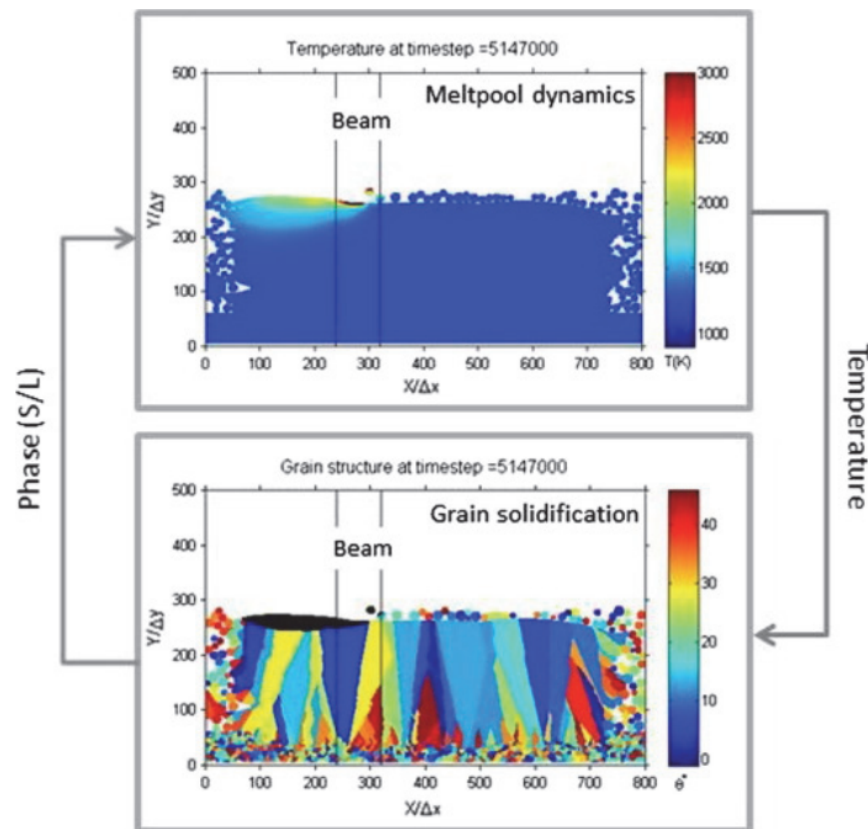


**FIG. 11:** Temperature field and the resulting grain structure calculated using the CALB model (Reprinted with permission from Elsevier, Copyright 2016)<sup>103</sup>

$$m_i \ddot{\mathbf{r}}_i = \Psi_i^{\text{con}} + \Psi_i^{\text{wall}} + \Psi_i^{\text{bond}} + \Psi_i^{\text{damp}} + \Psi_i^{e+m} \quad (31)$$

where  $m_i$  represents mass and  $\mathbf{r}_i$  represents the position of the  $i$ th particle in the domain.  $\Psi^{\text{con}}$ ,  $\Psi^{\text{wall}}$ ,  $\Psi^{\text{bond}}$ ,  $\Psi^{\text{damp}}$ , and  $\Psi^{e+m}$  represents contact force generated through contact with other particles (Fig. 12),<sup>109</sup> wall force generated through contact with constraining surfaces, adhesive bonding force, damping force arising from the surrounding interstitial environment and electromagnetic force respectively. The thermal governing equation is given by

$$Q_i + H_i = m_i C_i \dot{\theta}_i, \quad H_i = \alpha_i I_i V_i \quad (32)$$

where  $Q$  represents the conductive contribution from surrounding particles in contact,  $H$  is a source term representing heat input from the laser,  $m$  is mass,  $C$  is the heat capacity of the material,  $\theta$  is the temperature,  $\alpha$  is the absorption coefficient,  $I$  is the intensity of laser heat source and  $V$  is the velocity of laser heat source. In the discrete particle method, physics is strongly coupled. The dynamic model dictates the contact of particles by considering contact forces also controls the conductive heat transfer and resulting thermal field.

Zohdi<sup>106</sup> explained the detailed algorithm to solve this strongly coupled system iteratively. Various methods to model heat sources in numerical modeling are also mentioned. Some methods were computationally very expensive while others were very simple for the approximation of heat source. Therefore, modeling of heat sources through the Beer-Lambert law was recommended. Lee and Zhang<sup>107</sup> used the discrete element method to include the influences of a random powder bed and coupled it with the 3D continuum model to simulate the melt-pool dynamics without incorporating evaporation. Furthermore, Wu et al.<sup>108</sup> considered evaporation of material and found that the melt pool becomes deeper and narrower and surface temperature becomes lower (Fig. 13). The surface morphologies are different by considering the evaporation in the material.

### 3. DATA-DRIVEN MACHINE LEARNING (ML) MODELING

#### 3.1 ML Diagnosis of Melt-Pool Dynamics

As introduced in Section 1.4, the rich in-process data in metal AM provides an opportunity to develop alternative data-driven ML models to overcome the inherent problems associated with physics-based computational models. This prompted the integration of ML

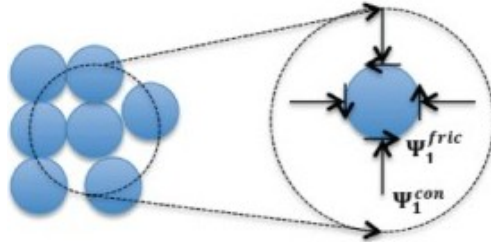


**FIG. 12:** Normal force and friction force on the particles (Reprinted with permission from Elsevier, Copyright 2014)<sup>109</sup>

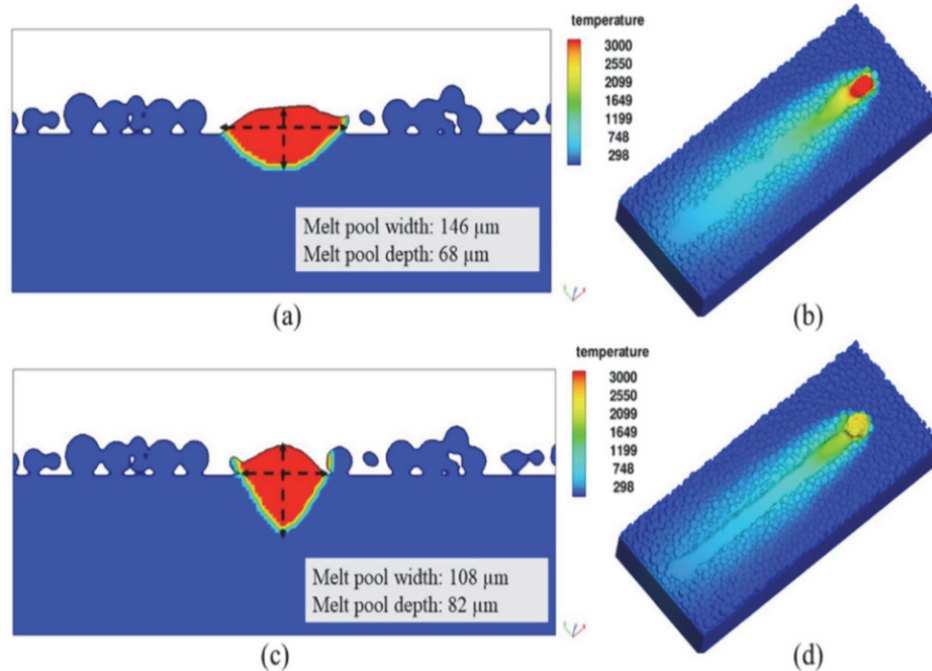


**FIG. 13:** (a) The melt pool is wide and shallow when neglecting evaporation, (b) the temperature of the melt pool overheating, (c) the melt pool is narrow and deep when incorporating evaporation, and (d) the maximum temperature is 2676 K when evaporation occurs (Reprinted with permission from Elsevier, Copyright 2018)<sup>108</sup>

techniques to metal AM workflow and leverage data analytics enabled by integrated the internet-of-things sensors for process diagnosis. Table 3<sup>110–130</sup> summarizes the key thermal data acquisition methods, the implementation of ML architectures [e.g., convolutional neural network (CNN), deep neural network (DNN), and support vector machine (SVM)], and the predicted key parameters of melt-pool dynamics (e.g., shape, size, temperature, pressure, and velocity).

### 3.2 ML Prognosis of Melt-Pool Dynamics

The unique combination of rapid heating and cooling cycles in the metal pool generates an extreme dynamic behavior that is not encountered in conventional manufacturing processes. Also, more than 50 aleatorically uncertain process parameters (e.g., laser power random variation) affect the fluid and phase-change process dynamics, collectively leading to a locally nonuniform melt pool (e.g., overheating near fine geometric features), which may lead to poor part quality (e.g., porosity). Understanding, prediction, and real-time control of melt-pool dynamics remains a central challenge for printing high-quality functional metal parts. Physics-based computational models require model parameter calibration and are also computationally expensive.<sup>40,131</sup> These deterministic models may not

**TABLE 3:** ML models for PBF melt pool diagnosis

Sensor type	Data acquisition	ML model	Predictions	Refs.
IR camera	Melt pool temperatures	Self-organizing NN	Microstructure defects	110
Thermographic camera	Thermographic images	CNN	Delamination	111
Digital single-lens reflex (DSLR) camera	Powder bed images	Deep-CNN	Process anomaly	112, 113
DSLR camera	Layer wise images	SVM	Solidification discontinuities	114, 115
High-speed camera	Melt pool images	CNN	Pores	116
Two-color pyrometer and CMOS camera	Melt pool images	Nearest-neighbor classification ML	Pores	117
Photodiode	Thermal radiation	Gaussian mixture model	Build category	118
High-speed camera	Melt pool images	CNN	Build category and anomaly	119, 120
Near IR camera	Plume and splatter signatures	CNN	Melt pool status	121
High-speed camera	Melt pool images	SIFT and BOW	Keyhole	122
DSLR camera	Powder bed images	DNN	Pores	122, 123
Photodiode sensor and short-wave IR camera	Melt-pool images	CNN	Melt pool status	124
High-speed camera	Melt-pool images	SVM, CNN, DNN	Pores	125, 126
High-speed camera	Melt-pool images	Hybrid SVM-CNN	Pores	127
High-speed camera	Melt pool size	DNN	Printing defects	128
Pyrometer	Melt pool image	SVM, KNN, SNN	Pores	129
High-speed X-ray and IR camera	Melt pool thermal history	GPC, RFC, GBC	Pores	130



incorporate actual process dynamics due to process variations and uncertainty. Furthermore, the unknown nonlinearities and rapidly changing behavior (e.g., overheating) are challenging for control systems.

On the other hand, the available online process data of the melt pool account for process dynamics in real time. ML has great potential to learn and/or even discover the governing equations underlying the melt-pool dynamics directly from the measured data and domain knowledge. Although initial development and training of such prognosis ML algorithms demand significant time and computational resources, once ML models are trained they can enable real-time predictive optimization and corrective actions for complex SLM build processes, which may be many times faster than physics-based computational models. While the scope for melt prognosis-focused ML models is huge, defect prediction and process control will still be the focus in the coming years to attain greater PBF process reliability. Unsupervised learning models prove most suitable for PBF melt-pool predictive analytics. Table 4<sup>132–135</sup> summarizes several ML cases for melt-pool prognosis.

### 3.3 Physics-Informed ML

Although data science (e.g., ML, DL) models harness process data through real-time sensing in metal AM processes, the outcomes of these models often lack physical meaning, transparency, and explainability. On the other hand, computational models are based on physical principles underpinning metal AM processes, therefore providing explicit insights into the process phenomena. However, physical models are often simplified with assumptions to reduce modeling complexity and computation cost. Furthermore, offline computational models are inherently not suited for incorporating real-time process data, therefore missing the real-time process variations and uncertainties. The integration of physical laws and domain knowledge into ML will forge a PIML method to leverage the complementary advantages of both physical and data-driven models. PIML may significantly improve the accuracy and reliability with enhanced transparency and explainability.

**TABLE 4:** ML models for PBF melt pool prognosis

Sensor type	Data acquisition	ML model	Predictions	Refs.
IR camera, X-ray CT pyrometer	Melt pool images	NN, CNN	Real-time porosity	132
IR camera	Melt pool size	PINN, DNN	Temperature pressure, and velocity of melt pool	133
Optical metallographs	Melt pool geometry	NN, SVM	Shape of melt pool	134
Camera, pyrometer acoustic sensor	Melt pool video	CNN	Solidified track width	135

In a dynamic metal AM system, the relationships among the process variables follow, albeit complex or even intractable, strict physics laws. The model learned from ML should satisfy these physical constraints or side information (e.g., partially known physical system information or properties); otherwise, it may generate misleading results. However, a vast amount of prior knowledge exists that is currently not being utilized in modern ML practice. This prior/side information can act as a regularization agent that constrains the space of admissible solutions of ML to a manageable size or leans toward the ground truth (e.g., using sparsity) over other plausible solutions. In return, encoding such structured information into a learning algorithm may help construct data-efficient and physics-informed ML techniques.<sup>136–141</sup>

A recent PIML has been developed to predict the melt pool fluid dynamics in selective laser melting.<sup>133</sup> The results show that the PIML can accurately predict temperature, pressure, and velocity field without relying on big data. A hard approach was used to impose the Dirichlet boundary condition with the prescribed value and speed up the learning process. However, this PIML model did not resolve the ambient gas phase, free-surface deformation of the melt pool, and the evaporation phenomenon. The multiphase Navier-Stokes could be enhanced with the evaporation model in the momentum equations, which was used in the control volume finite element model,<sup>142</sup> to capture the heat loss, composition change, and fluid motion induced by evaporation. Additional PDEs, such as the convection equation of level set or VOF used in the literature,<sup>143</sup> may be incorporated into PIML to enable a modeling metal AM process at the powder scale.

## 4. SUMMARY AND OUTLOOK

### 4.1 Multiscale Physical Modeling of Dynamic Metal AM

Physics-based computational methods, including CFD, FVM, FEM, LBM, and DMP, are enabling tools to understand insights into various metal AM process phenomena and predict process parameters at different scales. However, the conventional physics-based computational models have four inherent issues, as follows:

- I. These models are based on assumptions, simplifications, and approximations.
- II. The model coefficients require a continuous update to account for the highly nonlinear process dynamics and uncertainty.
- III. The computational cost is exceedingly high due to the involved nonlinear equations and multi-physics (e.g., thermal–fluid–mechanical coupling).
- IV. It is very challenging to bridge respective physical models across different scales.

Therefore, the development of a unified and efficient computational model crossing different temporal and spatial scales is valuable for predicting various process phenomena and parameters at different scales.

## 4.2 Thermophysical Properties at Different Scales

The fidelity of physics-based computational methods is highly dependent on the thermophysical properties of materials at different stages, from particles, melt pool, solidification, and bulk. Current models use either assumed constants or simplified values. The pressing issue is that the material-related model coefficients change with the material state.

## 4.3 Data Availability

The available sufficient data are critical for training a ML model or updating coefficients of a physics-based model. Online process sensing and monitoring of metal AM are finding slow, as most metal printers are not equipped with *in situ* sensors. Despite many sensing techniques developed to gather data from a printing process, there are still large roadblocks toward applying the sensing techniques [e.g., pyrometry and infrared (IR) camera] for reliable real-time monitoring, such as sensor fusion to allow for a deeper understanding of an AM process, massive data processing, and correlation of multi-sensor signals in real time. Data integrity is another consideration, because any ML model can be sabotaged by poor-quality training data under the colloquial “garbage in, garbage out” paradigm. Data collected are often noisy, redundant, or incomplete, and therefore of low quality, offering limited useful information from which to learn.

## 4.4 Conventional ML Modeling with Large Training Data

The pervasive process data provides an opportunity to integrate physical knowledge (e.g., first principles) with data (e.g., either simulated and/or measured) at respective scales, which allows the development of hybrid physical/data-driven ML models at different scales. ML is naturally easy to integrate, multimodality data crossing different scales for bridging process features (e.g., particle, melt pool, and part) at different scales. Each physics-informed ML model captures the process phenomena at a different scale. The multiscale model may be trained iteratively via localization (i.e., mapping of quantities at high scale to quantities at low scale) and homogenization (i.e., mapping of quantities at low scale to quantities at high scale).

## 4.5 PIML Modeling with Small Data

The conventional pure-data-driven ML model needs massive data for training to predict reasonably accurate results. The concept of PIML has been initiated, but at an early stage. Encoding mathematical physics of metal AM processes and structured information (e.g., domain knowledge) into an ML algorithm by regulating the loss function will not only quickly predict an accurate solution but also only requires a small amount of training data. Furthermore, ML acceleration techniques, such as structured neural network model compression and dynamic inference and training schemes, may further reduce the time latency of training a ML model.

## ACKNOWLEDGMENT

The authors thank the financial support of DOE/CyManII under Grant No. 829552.

## REFERENCES

1. ASTM, Standard Terminology for Additive Manufacturing Technologies: Designation F2792-12a, ASTM Int., West Conshohocken, PA, 2012.
2. ASTM, Additive Manufacturing—General Principle—Terminology, ASTM Int., West Conshohocken, PA, 2016.
3. Deckard, C.R., Method and Apparatus for Producing Parts by Selective Sintering, Google Patents, Patent No. 4863538, 1989.
4. Meiners, W., Wissenbach, K., and Gasser, A., Shaped Body Especially Prototype or Replacement Part Production, Patent No. DE19649865C1, 1998.
5. Larson, R., Method and Device for Producing Three-Dimensional Bodies, Google Patents, Patent No. 5786562, 1998.
6. Griffith, M., Keicher, D., and Atwood, C.L., Free Form Fabrication of Metallic Components Using Laser Engineered Net Shaping (LENS {Trademark}), Sandia National Labs., Albuquerque, 1996.
7. Mertens, R., Clijsters, S., Kempen, K., and Kruth, J.-P., Optimization of Scan Strategies in Selective Laser Melting of Aluminum Parts with Downfacing Areas, *J. Manuf. Sci. Eng.*, vol. **136**, no. 6, p. 061012, 2014.
8. Sidambe, A.T., Biocompatibility of Advanced Manufactured Titanium Implants—A Review, *Materials*, vol. **7**, no. 12, pp. 8168–8188, 2014.
9. Atwood, C., Griffith, M., Harwell, L., Schlienger, E., Ensiz, M., Smugeresky, J., Romero, T., Greene, D., and Reckaway, D., Eds., Laser Engineered Net Shaping (LENS<sup>TM</sup>): A Tool for Direct Fabrication of Metal Parts, *Proc. of Int. Congress on Applications of Lasers & Electro-Optics*, Laser Institute of America, Orlando, pp. E1–E7, 1998.
10. Jaluria, Y., Microscale Transport Phenomena in Materials Processing, *J. Heat Transf.*, vol. **131**, no. 3, p. 033111, 2009.
11. Jaluria, Y., Thermal Issues in Materials Processing, *J. Heat Transf.*, vol. **135**, no. 6, p. 061004, 2013.
12. Jaluria, Y., Heat and Mass Transfer in Materials Processing and Manufacturing, *Adv. Heat Transf.*, vol. **48**, pp. 1–94, 2016.
13. Poulikakos, D. and Waldvogel, J.M., Heat Transfer and Fluid Dynamics in the Process of Spray Deposition, *Adv. Heat Transf.*, vol. **28**, pp. 1–74, 1996.
14. Kou, S., *Transport Phenomena and Materials Processing*, Hoboken, NJ: Wiley, 1996.
15. Jaluria, Y., *Advanced Materials Processing and Manufacturing*, Berlin: Springer, 2018.
16. Jaluria, Y., *Design and Optimization of Thermal Systems*, Boca Raton, FL: CRC Press, 2007.
17. Fu, C. and Guo, Y., Three-Dimensional Temperature Gradient Mechanism in Selective Laser Melting of Ti-6Al-4V, *J. Manuf. Sci. Eng.*, vol. **136**, no. 6, p. 061004, 2014.
18. Craeghs, T., Clijsters, S., Yasa, E., Bechmann, F., Berumen, S., and Kruth, J.-P., Determination of Geometrical Factors in Layerwise Laser Melting Using Optical Process Monitoring, *Opt. Lasers Eng.*, vol. **49**, no. 12, pp. 1440–1446, 2011.

19. Craeghs, T., Clijsters, S., Kruth, J.-P., Bechmann, F., and Ebert, M.-C., Detection of Process Failures in Layerwise Laser Melting with Optical Process Monitoring, *Phys. Procedia*, vol. **39**, pp. 753–759, 2012.
20. Heigel, J.C. and Whittenon, E., Eds., Measurement of Thermal Processing Variability in Powder Bed Fusion, *Proc. of 2018 ASPE and Euspen Summer Topical Meeting-Advancing Precision in Additive Manufacturing*, Am. Soc. Precision Eng., Albany, pp. 22–25, 2018.
21. Lane, B., Whittenon, E., and Moylan, S., Eds., Multiple Sensor Detection of Process Phenomena in Laser Powder Bed Fusion, *Thermosense: Therm. Inf. Appl. XXXVIII*, vol. **9861**, pp. 20–28, 2016.
22. Li, C., Fu, C., Guo, Y., and Fang, F., A Multiscale Modeling Approach for Fast Prediction of Part Distortion in Selective Laser Melting, *J. Mater. Process. Technol.*, vol. **229**, pp. 703–712, 2016.
23. Li, C., Liu, J., Fang, X., and Guo, Y., Efficient Predictive Model of Part Distortion and Residual Stress in Selective Laser Melting, *Additive Manuf.*, vol. **17**, pp. 157–168, 2017.
24. Li, C., Guo, Y., Fang, X., and Fang, F., A Scalable Predictive Model and Validation for Residual Stress and Distortion in Selective Laser Melting, *CIRP Ann.*, vol. **67**, no. 1, pp. 249–252, 2018.
25. Li, C., Liu, Z., Fang, X., and Guo, Y., On the Simulation Scalability of Predicting Residual Stress and Distortion in Selective Laser Melting, *J. Manuf. Sci. Eng.*, vol. **140**, no. 4, p. 041013, 2018.
26. Strantza, M., Ganeriwala, R.K., Clausen, B., Phan, T.Q., Levine, L.E., Pagan, D., King, W.E., Hodge, N.E., and Brown, D.W., Coupled Experimental and Computational Study of Residual Stresses in Additively Manufactured Ti-6Al-4V Components, *Mater. Lett.*, vol. **231**, pp. 221–224, 2018.
27. Li, C., Guo, Y., and Zhao, J., Interfacial Phenomena and Characteristics between the Deposited Material and Substrate in Selective Laser Melting Inconel 625, *J. Mater. Process. Technol.*, vol. **243**, pp. 269–281, 2017.
28. Li, C., White, R., Fang, X., Weaver, M., and Guo, Y., Microstructure Evolution Characteristics of Inconel 625 Alloy from Selective Laser Melting to Heat Treatment, *Mater. Sci. Eng., A*, vol. **705**, pp. 20–31, 2017.
29. Wang, M., Li, H., Lou, D., Qin, C., Jiang, J., Fang, X., and Guo, Y., Microstructure Anisotropy and Its Implication in Mechanical Properties of Biomedical Titanium Alloy Processed by Electron Beam Melting, *Mater. Sci. Eng., A*, vol. **743**, pp. 123–137, 2019.
30. Holland, S., Wang, X., Fang, X., Guo, Y., Yan, F., and Li, L., Grain Boundary Network Evolution in Inconel 718 from Selective Laser Melting to Heat Treatment, *Mater. Sci. Eng., A*, vol. **725**, pp. 406–418, 2018.
31. Kok, Y., Tan, X.P., Wang, P., Nai, M., Loh, N.H., Liu, E., and Tor, S.B., Anisotropy and Heterogeneity of Microstructure and Mechanical Properties in Metal Additive Manufacturing: A Critical Review, *Mater. Des.*, vol. **139**, pp. 565–586, 2018.
32. Minkowycz, W., Sparrow, E., and Murthy, J., *Handbook of Numerical Heat Transfer*, Hoboken, NJ: Wiley, 2006.
33. Jaluria, Y. and Torrance, K.E., *Computational Heat Transfer*, Boca Raton, FL: Routledge, 2017.

34. Anderson, D., Tannehill, J.C., and Pletcher, R.H., *Computational Fluid Mechanics and Heat Transfer*, Boca Raton, FL: Routledge, 2016.
35. Shyy, W., Udaykumar, H., Rao, M.M., and Smith, R.W., *Computational Fluid Dynamics with Moving Boundaries*, Mineola, NY: Dover, 1996.
36. Meier, C., Penny, R.W., Zou, Y., Gibbs, J.S., and Hart, A.J., Thermophysical Phenomena in Metal Additive Manufacturing by Selective Laser Melting: Fundamentals, Modeling, Simulation and Experimentation, *Ann. Rev. Heat Transf.*, vol. **20**, pp. 241–316, 2018.
37. Teng, C., Gong, H., Szabo, A., Dilip, J.J.S., Ashby, K., Zhang, S., Patil, N., Pal, D., and Stucker, B., Simulating Melt Pool Shape and Lack of Fusion Porosity for Selective Laser Melting of Cobalt Chromium Components, *J. Manuf. Sci. Eng.*, vol. **139**, no. 1, p. 011009, 2016.
38. Deng, J., Dong, W., Socher, R., Li, L.-J., Li, K., and Fei-Fei, L., Eds., Imagenet: A Large-Scale Hierarchical Image Database, *2009 IEEE Conf. on Computer Vision and Pattern Recognition*, Miami, pp. 248–255, 2009.
39. Tian, Q., Guo, S., and Guo, Y., A Physics-Driven Deep Learning Model for Process-Porosity Causal Relationship and Porosity Prediction with Interpretability in Laser Metal Deposition, *CIRP Annals*, vol. **69**, no. 1, pp. 205–208, 2020.
40. Karpatne, A., Atluri, G., Faghmous, J.H., Steinbach, M., Banerjee, A., Ganguly, A., Shekhar, S., Samatova, N., and Kumar, V., Theory-Guided Data Science: A New Paradigm for Scientific Discovery from Data, *IEEE Trans. Knowl. Data Eng.*, vol. **29**, no. 10, pp. 2318–2331, 2017.
41. Clijsters, S., Craeghs, T., and Kruth, J.-P., A Priori Process Parameter Adjustment for SLM Process Optimization, *Proc. of VRAP Int. Conf. Advanced Research in Virtual and Rapid Prototyping*, Leiria, Portugal, pp. 553–560, 2012.
42. Depond, P.J., Guss, G., Ly, S., Calta, N.P., Deane, D., Khairallah, S., and Matthews, M.J., *In Situ* Measurements of Layer Roughness During Laser Powder Bed Fusion Additive Manufacturing Using Low Coherence Scanning Interferometry, *Mater. Des.*, vol. **154**, pp. 347–359, 2018.
43. Mani, M., Feng, S., Brandon, L., Donmez, A., Moylan, S., and Fesperman, R., *Measurement Science Needs for Real-Time Control of Additive Manufacturing Powder-Bed Fusion Processes*, Boca Raton, FL: CRC Press, 2017.
44. Monostori, L., Márkus, A., Van Brussel, H., and Westkämpfer, E., Machine Learning Approaches to Manufacturing, *CIRP Ann.*, vol. **45**, no. 2, pp. 675–712, 1996.
45. Voyant, C., Notton, G., Kalogirou, S., Nivet, M.-L., Paoli, C., Motte, F., and Fouilloy, A., Machine Learning Methods for Solar Radiation Forecasting: A Review, *Renew. Energy*, vol. **105**, pp. 569–582, 2017.
46. Johnson, N.S., Vulimiri, P.S., To, A.C., Zhang, X., Brice, C.A., Kappes, B.B., and Stebner, A.P., Invited Review: Machine Learning for Materials Developments in Metals Additive Manufacturing, *Additive Manuf.*, vol. **36**, p. 101641, 2020.
47. Tarsha-Kurdi, F., Landes, T., Grussenmeyer, P., and Koehl, M., Eds., Model-Driven and Data-Driven Approaches Using Lidar Data: Analysis and Comparison, in *ISPRS Workshop, Photogrammetric Image Analysis (PIA07)*, Munich, pp. 87–92, 2007.
48. Wang, J., Chang, Q., Xiao, G., Wang, N., and Li, S., Data Driven Production Modeling and

- Simulation of Complex Automobile General Assembly Plant, *Comput. Ind.*, vol. **62**, no. 7, pp. 765–775, 2011.
49. Pozdnoukhov, A., Foresti, L., and Kanevski, M., Data-Driven Topo-Climatic Mapping with Machine Learning Methods, *Nat. Haz.*, vol. **50**, no. 3, pp. 497–518, 2009.
  50. Swischuk, R., Mainini, L., Peherstorfer, B., and Willcox, K., Projection-Based Model Reduction: Formulations for Physics-Based Machine Learning, *Comput. Fluids*, vol. **179**, pp. 704–717, 2019.
  51. Schlimmer, J.C. and Granger, R.H., Incremental Learning from Noisy Data, *Mach. Learn.*, vol. **1**, no. 3, pp. 317–354, 1986.
  52. Moore, J.L., Dickson-Deane, C., and Galyen, K., E-Learning, Online Learning, and Distance Learning Environments: Are They the Same?, *Internet High. Educ.*, vol. **14**, no. 2, pp. 129–135, 2011.
  53. Meier, C., Penny, R., Zou, Y., Gibbs, J., and Hart, A., Thermophysical Phenomena in Metal Additive Manufacturing by Selective Laser Melting: Fundamentals, Modeling, Simulation and Experimentation, *Ann. Rev. Heat Transf.*, vol. **20**, pp. 241–316, 2018.
  54. Tseng, C.-C. and Li, C.-J., Numerical Investigation of Interfacial Dynamics for the Melt Pool of Ti-6Al-4V Powders under a Selective Laser, *Int. J. Heat Mass Transf.*, vol. **134**, pp. 906–919, 2019.
  55. Verhaeghe, F., Craeghs, T., Heulens, J., and Pandelaers, L., A Pragmatic Model for Selective Laser Melting with Evaporation, *Acta Mater.*, vol. **57**, no. 20, pp. 6006–6012, 2009.
  56. Panwisawas, C., Qiu, C., Sovani, Y., Brooks, J., Attallah, M., and Basoalto, H., On the Role of Thermal Fluid Dynamics into the Evolution of Porosity during Selective Laser Melting, *Scripta Mater.*, vol. **105**, pp. 14–17, 2015.
  57. Panwisawas, C., Qiu, C., Anderson, M.J., Sovani, Y., Turner, R.P., Attallah, M.M., Brooks, J.W., and Basoalto, H.C., Mesoscale Modelling of Selective Laser Melting: Thermal Fluid Dynamics and Microstructural Evolution, *Comput. Mater. Sci.*, vol. **126**, pp. 479–490, 2017.
  58. Li, C.-J., Tsai, T.-W., and Tseng, C.-C., Numerical Simulation for Heat and Mass Transfer during Selective Laser Melting of Titanium Alloys Powder, *Phys. Procedia*, vol. **83**, pp. 1444–1449, 2016.
  59. Otto, A., Koch, H., Leitz, K.-H., and Schmidt, M., Numerical Simulations—A Versatile Approach for Better Understanding Dynamics in Laser Material Processing, *Phys. Procedia*, vol. **12**, pp. 11–20, 2011.
  60. Francois, M., A Study of the Volume of Fluid Method for Moving Boundary Problems, Msae, Embry-Riddle Aeronautical University, Ann Arbor, 1998.
  61. Cheng, B., Loeber, L., Willeck, H., Hartel, U., and Tuffile, C., Computational Investigation of Melt Pool Process Dynamics and Pore Formation in Laser Powder Bed Fusion, *J. Mater. Eng. Perform.*, vol. **28**, no. 11, pp. 6565–6578, 2019.
  62. Gürtler, F.J., Karg, M., Leitz, K.H., and Schmidt, M., Simulation of Laser Beam Melting of Steel Powders Using the Three-Dimensional Volume of Fluid Method, *Phys. Procedia*, vol. **41**, pp. 881–886, 2013.
  63. De Baere, D., Bayat, M., Mohanty, S., and Hattel, J., Thermo-Fluid-Metallurgical Modelling of the Selective Laser Melting Process Chain, *Procedia CIRP*, vol. **74**, pp. 87–91, 2018.

64. Zhou, Y.H., Zhang, Z.H., Wang, Y.P., Liu, G., Zhou, S.Y., Li, Y.L., Shen, J., and Yan, M., Selective Laser Melting of Typical Metallic Materials: An Effective Process Prediction Model Developed by Energy Absorption and Consumption Analysis, *Additive Manuf.*, vol. **25**, pp. 204–217, 2019.
65. Fu, C.H., Guo, Y.B., and Sealy, M.P., A Predictive Model and Validation of Laser Cutting of Nitinol with a Novel Moving Volumetric Pulsed Heat Flux, *J. Mater. Process. Technol.*, vol. **214**, no. 12, pp. 2926–2934, 2014.
66. Yang, J., Sun, S., Brandt, M., and Yan, W., Experimental Investigation and 3D Finite Element Prediction of the Heat Affected Zone during Laser Assisted Machining of Ti6Al4V Alloy, *J. Mater. Process. Technol.*, vol. **210**, no. 15, pp. 2215–2222, 2010.
67. Lee, S.H., Analysis of Precision Deburring Using a Laser—An Experimental Study and Fem Simulation, *KSME Int. J.*, vol. **14**, no. 2, pp. 141–151, 2000.
68. Neela, V. and De, A., Three-Dimensional Heat Transfer Analysis of LENS TM Process Using Finite Element Method, *Int. J. Adv. Manuf. Technol.*, vol. **45**, no. 9, pp. 935–943, 2009.
69. Wang, Y.-Z. and Lin, J., Characterization of the Laser Cleaving on Glass Sheets with a Line-Shape Laser Beam, *Opt. Laser Technol.*, vol. **39**, no. 5, pp. 892–899, 2007.
70. Yilbas, B., Arif, A., and Karatas, C., Laser Gas Assisted Nitriding of Ti–6Al–4V Alloy and Residual Stress Analysis, *Surf. Eng.*, vol. **25**, no. 3, pp. 228–234, 2009.
71. Shuja, S., Yilbas, B., and Momin, O., Laser Heating of a Moving Slab: Influence of Laser Intensity Parameter and Scanning Speed on Temperature Field and Melt Size, *Opt. Laser Eng.*, vol. **49**, pp. 265–272, 2011.
72. Luo, Y., You, G., Ye, H., and Liu, J., Simulation on Welding Thermal Effect of AZ61 Magnesium Alloy Based on Three-Dimensional Modeling of Vacuum Electron Beam Welding Heat Source, *Vacuum*, vol. **84**, no. 7, pp. 890–895, 2010.
73. Zain-UI-Abdein, M., Nlias, D., Jullien, J.-F., and Deloison, D., Experimental Investigation and Finite Element Simulation of Laser Beam Welding Induced Residual Stresses and Distortions in Thin Sheets of AA 6056-T4, *Mater. Sci. Eng., A*, vol. **527**, no. 12, pp. 3025–3039, 2010.
74. Xuan, F.-Z., Cao, L.-Q., Wang, Z., and Tu, S.-T., Mass Transport in Laser Surface Nitriding Involving the Effect of High Temperature Gradient: Simulation and Experiment, *Comput. Mater. Sci.*, vol. **49**, no. 1, pp. 104–111, 2010.
75. Hussein, A., Hao, L., Yan, C., and Everson, R., Finite Element Simulation of the Temperature and Stress Fields in Single Layers Built Without-Support in Selective Laser Melting, *Mater. Des. (1980–2015)*, vol. **52**, pp. 638–647, 2013.
76. Wang, Z., Denlinger, E., Michaleris, P., Stoica, A.D., Ma, D., and Beese, A.M., Residual Stress Mapping in Inconel 625 Fabricated through Additive Manufacturing: Method for Neutron Diffraction Measurements to Validate Thermomechanical Model Predictions, *Mater. Des.*, vol. **113**, pp. 169–177, 2017.
77. Roberts, I.A., Wang, C., Esterlein, R., Stanford, M., and Mynors, D., A Three-Dimensional Finite Element Analysis of the Temperature Field during Laser Melting of Metal Powders in Additive Layer Manufacturing, *Int. J. Mach. Tools Manuf.*, vol. **49**, nos. 12–13, pp. 916–923, 2009.
78. Zaeh, M.F., Branner, G., and Krol, T.A., A Three Dimensional FE-Model for the Investigation of Transient Physical Effects in Selective Laser Melting, *Proc of 4th Int. Conf. on Advanced*



- Research in Virtual and Rapid Prototyping: Innovative Development in Design and Manufacturing*, Leiria, Portugal, pp. 415–424, 2009.
79. Li, C., Wang, Y., Zhan, H., Han, T., Han, B., and Zhao, W., Three-Dimensional Finite Element Analysis of Temperatures and Stresses in Wide-Band Laser Surface Melting Processing, *Mater. Des.*, vol. **31**, no. 7, pp. 3366–3373, 2010.
  80. Saxena, S., Sharma, R., and Kumar, A., A Microscale Study of Thermal Field and Stresses During Processing of Ti6Al4V Powder Layer by Selective Laser Melting, *Lasers Manuf. Mater. Process.*, vol. **5**, pp. 265–272, 2018.
  81. Childs, T., Hauser, C., and Badrossamay, M., Mapping and Modelling Single Scan Track Formation in Direct Metal Selective Laser Melting, *CIRP Ann.*, vol. **53**, no. 1, pp. 191–194, 2004.
  82. Zhang, D.Q., Cai, Q.Z., Liu, J.H., Zhang, L., and Li, R.D., Select Laser Melting of W–Ni–Fe Powders: Simulation and Experimental Study, *Int. J. Adv. Manuf. Technol.*, vol. **51**, no. 5, pp. 649–658, 2010.
  83. Shiomi, M., Osakada, K., Nakamura, K., Yamashita, T., and Abe, F., Residual Stress Within Metallic Model Made by Selective Laser Melting Process, *CIRP Ann.*, vol. **53**, no. 1, pp. 195–198, 2004.
  84. Li, J.F., Li, L., and Stott, F.H., Thermal Stresses and Their Implication on Cracking during Laser Melting of Ceramic Materials, *Acta Mater.*, vol. **52**, no. 14, pp. 4385–4398, 2004.
  85. Nickel, A.H., Barnett, D.M., and Prinz, F.B., Thermal Stresses and Deposition Patterns in Layered Manufacturing, *Mater. Sci. Eng., A*, vol. **317**, no. 1, pp. 59–64, 2001.
  86. Hodge, N., Ferencz, R.M., and Solberg, J.M., Implementation of a Thermomechanical Model in Diablo for the Simulation of Selective Laser Melting, Lawrence Livermore National Lab Tech. Rep. LLNL-TR-644936, 2013.
  87. Aggarangsi, P. and Beuth, J., Localized Preheating Approaches for Reducing Residual Stress in Additive Manufacturing, *Proc. SFF Symp.*, Austin, pp. 709–720, 2006.
  88. Dai, K. and Shaw, L., Thermal and Stress Modeling of Multi-Material Laser Processing, *Acta Mater.*, vol. **49**, no. 20, pp. 4171–4181, 2001.
  89. Zaeh, M.F. and Branner, G., Investigations on Residual Stresses and Deformations in Selective Laser Melting, *Product. Eng.*, vol. **4**, no. 1, pp. 35–45, 2010.
  90. Krol, T., Westhäuser, S., Zäh, M., Schilp, J., and Groth, G., Development of a Simulation-Based Process Chain—Strategy for Different Levels of Detail for the Preprocessing Definitions, *SNE Simul. Notes Eur.*, vol. **21**, pp. 135–140, 2011.
  91. Papadakis, L., Loizou, A., Risse, J., and Bremen, S., A Thermo-Mechanical Modeling Reduction Approach for Calculating Shape Distortion in SLM Manufacturing for Aero Engine Components, in *Proc. of the 6th Int. Conf. on Advanced Research in Virtual and Rapid Prototyping*, Leiria, Portugal, pp. 1–5, 2013.
  92. Papadakis, L., Loizou, A., Risse, J., and Schrage, J., Numerical Computation of Component Shape Distortion Manufactured by Selective Laser Melting, *Procedia CIRP*, vol. **18**, pp. 90–95, 2014.
  93. Ding, J., Colegrove, P., Mehnen, J., Ganguly, S., Almeida, P., Wang, F., and Williams, S., Thermomechanical Analysis of Wire and Arc Additive Layer Manufacturing Process on Large Multi-Layer Parts, *Comput. Mater. Sci.*, vol. **50**, pp. 3315–3322, 2011.

94. Körner, C., Attar, E., and Heintl, P., Mesoscopic Simulation of Selective Beam Melting Processes, *J. Mater. Process. Technol.*, vol. **211**, no. 6, pp. 978–987, 2011.
95. Zäh, M.F. and Lutzmann, S., Modelling and Simulation of Electron Beam Melting, *Product. Eng.*, vol. **4**, no. 1, pp. 15–23, 2010.
96. Fischer, P., Romano, V., Weber, H.P., Karapatis, N.P., Boillat, E., and Glardon, R., Sintering of Commercially Pure Titanium Powder with a Nd:YAG Laser Source, *Acta Mater.*, vol. **51**, no. 6, pp. 1651–1662, 2003.
97. Körner, C., Pohl, T., Rüde, U., Thürey, N., and Zeiser, T., Eds., *Parallel Lattice Boltzmann Methods for CFD Applications*, Berlin: Springer, 2006.
98. Markl, M. and Körner, C., Free Surface Neumann Boundary Condition for the Advection-Diffusion Lattice Boltzmann Method, *J. Comput. Phys.*, vol. **301**, pp. 230–246, 2015.
99. Attar, E. and Körner, C., Lattice Boltzmann Model for Thermal Free Surface Flows with Liquid–Solid Phase Transition, *Int. J. Heat Fluid Flow*, vol. **32**, no. 1, pp. 156–163, 2011.
100. Attar, E. and Körner, C., Lattice Boltzmann Method for Dynamic Wetting Problems, *J. Colloid Interface Sci.*, vol. **335**, no. 1, pp. 84–93, 2009.
101. Körner, C., Bauerei, A., and Attar, E., Fundamental Consolidation Mechanisms during Selective Beam Melting of Powders, *Model. Simul. Mater. Sci. Eng.*, vol. **21**, p. 085011, 2013.
102. Körner, C., Helmer, H., Bauerei, A., and Singer, R., Tailoring the Grain Structure of IN718 during Selective Electron Beam Melting, *Matec Web Conf.*, vol. **14**, p. 08001, 2014.
103. Rai, A., Markl, M., and Körner, C., A Coupled Cellular Automaton–Lattice Boltzmann Model for Grain Structure Simulation during Additive Manufacturing, *Comput. Mater. Sci.*, vol. **124**, pp. 37–48, 2016.
104. Luo, L.-S., Theory of the Lattice Boltzmann Method: Lattice Boltzmann Models for Nonideal Gases, *Phys. Rev. E*, vol. **62**, pp. 4982–4996, 2000.
105. Zohdi, T., A Direct Particle-Based Computational Framework for Electrically Enhanced Thermo-Mechanical Sintering of Powdered Materials, *Math. Mech. Solids*, vol. **19**, no. 1, pp. 93–113, 2014.
106. Zohdi, T.I., Additive Particle Deposition and Selective Laser Processing—A Computational Manufacturing Framework, *Comput. Mech.*, vol. **54**, no. 1, pp. 171–191, 2014.
107. Lee, Y. and Zhang, W., Mesoscopic Simulation of Heat Transfer and Fluid Flow in Laser Powder Bed Additive Manufacturing, in *2015 International Solid Freeform Fabrication Symposium*, Austin, pp. 1154–1165, 2015.
108. Wu, Y.-C., San, C.-H., Chang, C.-H., Lin, H.-J., Marwan, R., Baba, S., and Hwang, W.-S., Numerical Modeling of Melt-Pool Behavior in Selective Laser Melting with Random Powder Distribution and Experimental Validation, *J. Mater. Process. Technol.*, vol. **254**, pp. 72–78, 2018.
109. Ganeriwala, R. and Zohdi, T.I., Multiphysics Modeling and Simulation of Selective Laser Sintering Manufacturing Processes, *Procedia CIRP*, vol. **14**, pp. 299–304, 2014.
110. Jafari-Marandi, R., Khanzadeh, M., Tian, W., Smith, B., and Bian, L., From *In-Situ* Monitoring toward High-Throughput Process Control: Cost-Driven Decision-Making Framework for Laser-Based Additive Manufacturing, *J. Manuf. Syst.*, vol. **51**, pp. 29–41, 2019.
111. Baumgartl, H., Tomas, J., Buettner, R., and Merkel, M., A Deep Learning-Based Model

- for Defect Detection in Laser-Powder Bed Fusion Using *In-Situ* Thermographic Monitoring, *Prog. Add. Manuf.*, vol. **5**, pp. 277–285, 2020.
112. Caggiano, A., Zhang, J., Alfieri, V., Caiazzo, F., Gao, R., and Teti, R., Machine Learning-Based Image Processing for On-Line Defect Recognition in Additive Manufacturing, *CIRP Ann.*, vol. **68**, no. 1, pp. 451–454, 2019.
  113. Yadav, P., Singh, V.K., Joffre, T., Rigo, O., Arvieu, C., Le Guen, E., and Lacoste, E., Inline Drift Detection Using Monitoring Systems and Machine Learning in Selective Laser Melting, *Adv. Eng. Mater.*, vol. **22**, no. 12, p. 2000660, 2020.
  114. Gobert, C., Reutzel, E.W., Petrich, J., Nassar, A.R., and Phoha, S., Application of Supervised Machine Learning for Defect Detection during Metallic Powder Bed Fusion Additive Manufacturing Using High Resolution Imaging, *Additive Manuf.*, vol. **21**, pp. 517–528, 2018.
  115. Zur Jacobsmühlen, J., Kleszczynski, S., Witt, G., and Merhof, D., Eds., Detection of Elevated Regions in Surface Images from Laser Beam Melting Processes, *41st Annual Conf. of IEEE Industrial Electronics Soc.*, Yokohama, pp. 001270–001275, 2015.
  116. Zhang, B., Liu, S., and Shin, Y.C., In-Process Monitoring of Porosity during Laser Additive Manufacturing Process, *Additive Manuf.*, vol. **28**, pp. 497–505, 2019.
  117. Mitchell, J.A., Ivanoff, T.A., Dagel, D., Madison, J.D., and Jared, B., Linking Pyrometry to Porosity in Additively Manufactured Metals, *Additive Manuf.*, vol. **31**, p. 100946, 2020.
  118. Okaro, I.A., Jayasinghe, S., Sutcliffe, C., Black, K., Paoletti, P., and Green, P.L., Automatic Fault Detection for Laser Powder-Bed Fusion Using Semi-Supervised Machine Learning, *Additive Manuf.*, vol. **27**, pp. 42–53, 2019.
  119. Yang, Z., Lu, Y., Yeung, H., and Krishnamurthy, S., Eds., Investigation of Deep Learning for Real-Time Melt Pool Classification in Additive Manufacturing, *15th Int. Conf. on Automation Science and Engineering*, Vancouver, pp. 640–647, 2019.
  120. Scime, L. and Beuth, J., Melt Pool Geometry and Morphology Variability for the Inconel 718 Alloy in a Laser Powder Bed Fusion Additive Manufacturing Process, *Additive Manuf.*, vol. **29**, p. 100830, 2019.
  121. Ye, D., Fuh, J.Y.H., Zhang, Y., Hong, G.S., and Zhu, K., *In Situ* Monitoring of Selective Laser Melting Using Plume and Spatter Signatures by Deep Belief Networks, *ISA Trans.*, vol. **81**, pp. 96–104, 2018.
  122. Scime, L. and Beuth, J., Using Machine Learning to Identify *In-Situ* Melt Pool Signatures Indicative of Flaw Formation in a Laser Powder Bed Fusion Additive Manufacturing Process, *Additive Manuf.*, vol. **25**, pp. 151–165, 2019.
  123. Ertveldt, J., Guillaume, P., and Helsen, J., Miclad as a Platform for Real-Time Monitoring and Machine Learning in Laser Metal Deposition, *Procedia CIRP*, vol. **94**, pp. 456–461, 2020.
  124. Ren, Y.M., Zhang, Y., Ding, Y., Wang, Y., and Christofides, P.D., Computational Fluid Dynamics-Based *In-Situ* Sensor Analytics of Direct Metal Laser Solidification Process Using Machine Learning, *Comput. Chem. Eng.*, vol. **143**, p. 107069, 2020.
  125. Zhang, Y., Hong, G.S., Ye, D., Zhu, K., and Fuh, J.Y.H., Extraction and Evaluation of Melt Pool, Plume and Spatter Information for Powder-Bed Fusion AM Process Monitoring, *Mater. Des.*, vol. **156**, pp. 458–469, 2018.
  126. Kwon, O., Kim, H.G., Ham, M.J., Kim, W., Kim, G.-H., Cho, J.-H., Kim, N.I., and Kim, K., A Deep Neural Network for Classification of Melt-Pool Images in Metal Additive Manufacturing, *J. Intel. Manuf.*, vol. **31**, no. 2, pp. 375–386, 2020.

127. Zhang, Y., Soon, H.G., Ye, D., Fuh, J.Y.H., and Zhu, K., Powder-Bed Fusion Process Monitoring by Machine Vision with Hybrid Convolutional Neural Networks, *IEEE Trans. Indust. Inf.*, vol. **16**, no. 9, pp. 5769–5779, 2020.
128. Yeung, H., Yang, Z., and Yan, L., A Meltpool Prediction Based Scan Strategy for Powder Bed Fusion Additive Manufacturing, *Additive Manuf.*, vol. **35**, p. 101383, 2020.
129. Montazeri, M., Nassar, A.R., Dunbar, A.J., and Rao, P., In-Process Monitoring of Porosity in Additive Manufacturing Using Optical Emission Spectroscopy, *IJSE Trans.*, vol. **52**, no. 5, pp. 500–515, 2020.
130. Paulson, N.H., Gould, B., Wolff, S.J., Stan, M., and Greco, A.C., Correlations between Thermal History and Keyhole Porosity in Laser Powder Bed Fusion, *Additive Manuf.*, vol. **34**, p. 101213, 2020.
131. Guo, W.G., Tian, Q., Guo, S., and Guo, Y., A Physics-Driven Deep Learning Model for Process-Porosity Causal Relationship and Porosity Prediction with Interpretability in Laser Metal Deposition, *CIRP Annals*, 2020.
132. Jafari-Marandi, R., Khanzadeh, M., Tian, W., Smith, B., and Bian, L., From *In-Situ* Monitoring toward High-Throughput Process Control: Cost-Driven Decision-Making Framework for Laser-Based Additive Manufacturing, *J. Manuf. Syst.*, vol. **51**, pp. 29–41, 2019.
133. Zhu, Q., Liu, Z., and Yan, J., Machine Learning for Metal Additive Manufacturing: Predicting Temperature and Melt Pool Fluid Dynamics Using Physics-Informed Neural Networks, *Comput. Mech.*, vol. **67**, no. 2, pp. 619–635, 2021.
134. Lee, S., Peng, J., Shin, D., Choi, Y.S.J.S., and Materials, T.O.A., Data Analytics Approach for Melt-Pool Geometries in Metal, *Additive Manuf.*, vol. **20**, no. 1, pp. 972–978, 2019.
135. Yuan, B., Guss, G.M., Wilson, A.C., Hau-Riege, S.P., DePond, P.J., McMains, S., Matthews, M.J., and Giera, B., Machine-Learning-Based Monitoring of Laser Powder Bed Fusion, *Adv. Mater. Technol.*, vol. **3**, no. 12, p. 1800136, 2018.
136. Brunton, S.L., Proctor, J.L., and Kutz, J.N., Discovering Governing Equations from Data by Sparse Identification of Nonlinear Dynamical Systems, *Proc. Nat. Acad. Sci.*, vol. **113**, no. 15, pp. 3932–3937, 2016.
137. Brunton, S.L., Brunton, B.W., Proctor, J.L., Kaiser, E., and Kutz, J.N., Chaos as an Intermittently Forced Linear System, *Nat. Commun.*, vol. **8**, no. 1, pp. 1–9, 2017.
138. Rudy, S.H., Brunton, S.L., Proctor, J.L., and Kutz, J.N., Data-Driven Discovery of Partial Differential Equations, *Sci. Adv.*, vol. **3**, no. 4, p. e1602614, 2017.
139. Champion, K., Lusch, B., Kutz, J.N., and Brunton, S.L., Data-Driven Discovery of Coordinates and Governing Equations, *Proc. Nat. Acad. Sci.*, vol. **116**, no. 45, p. 22445, 2019.
140. Raissi, M., Perdikaris, P., and Karniadakis, G.E., Inferring Solutions of Differential Equations Using Noisy Multi-Fidelity Data, *J. Comput. Phys.*, vol. **335**, pp. 736–746, 2017.
141. Raissi, M., Perdikaris, P., and Karniadakis, G.E., Machine Learning of Linear Differential Equations Using Gaussian Processes, *J. Comput. Phys.*, vol. **348**, pp. 683–693, 2017.
142. Lin, S., Gan, Z., Yan, J., and Wagner, G.J., A Conservative Level Set Method on Unstructured Meshes for Modeling Multiphase Thermo-Fluid Flow in Additive Manufacturing Processes, *Comput. Methods Appl. Mech. Eng.*, vol. **372**, p. 113348, 2020.
143. Yan, J., Yan, W., Lin, S., and Wagner, G., A Fully Coupled Finite Element Formulation for Liquid–Solid–Gas Thermo-Fluid Flow with Melting and Solidification, *Comput. Methods Appl. Mech. Eng.*, vol. **336**, pp. 444–470, 2018.